



Mechanical and corrosion properties in 3.5% NaCl solution of cold sprayed Al-based coatings

Zhichao Zhang, Fuchun Liu*, En-Hou Han, Long Xu

Key Laboratory of Nuclear Materials and Safety Assessment, Institute of Metal Research, Chinese Academy of Sciences, Shenyang 110016, China
School of Materials Science and Engineering, University of Science and Technology of China, Hefei 230026, China



ARTICLE INFO

Keywords:

Cold spraying
Aluminum alloy coating
Components repair
Corrosion properties

ABSTRACT

The recent development of the cold spray method has made it possible to deposit dense coating with good adhesion and with almost no change in the microstructure, which is promising in repairing damaged Al-based aircraft skin. In this work, the in-situ shot-peening-assisted low-pressure cold spray method was used to deposit Al-based dense coatings with good mechanical and corrosion protection properties on AA 2024-T3 alloy. The detailed microstructure, coating adhesion, and corrosion protection performance were systematically investigated. A dense microstructure with low porosity (< 1.7%), high cohesive strength (> 45 MPa) is achieved for the coatings. By comparison, Al 5083 coating exhibited the optimum mechanical properties. The Al and Al 5083 coatings reveal similar pitting resistance and repassivation ability. During long-term immersion test (> 480 h) the corrosion resistance of Al 5083 coating surpassed that of CP Al coating. In conclusion, Al 5083 coating has a good combination of mechanical and anti-corrosion properties.

1. Introduction

Aluminum alloys, such as Al 2024, Al 5083, Al 7075, have been found important applications in the industry field due to their high specific strength, excellent strength-to-weight, good fracture toughness, and damage tolerance [1–5]. Meanwhile, it is well known that the alloying of Cu, Mg, Zn, and Mn in those alloys also significantly affects their corrosion behavior due to the electrochemical potential difference between the precipitate phases and the Al matrix [5–10].

Low-pressure cold spray (LPCS) method is a relatively newly developed technique for depositing coatings in solid state. During the spraying process, the metallic or dielectric substrate is exposed to a high velocity (300–1200 m s⁻¹) jet of small (1–50 µm) feedstock particles accelerated by a supersonic jet of compressed gas at a temperature lower than the melting point of the material [11–13]. Thus, oxidation, grain growth, residual tensile stress, phase changes and other typical drawbacks related to thermal spray can be avoided [14]. Since its low process temperature can minimize thermal stress and reduce the substrate deformation [15], cold spray is suitable for depositing not only a wide range of traditional and advanced materials on many types of substrate material, but also nontraditional applications which are sensitive to process temperature, especially for repairing damaged clad aluminum aircraft body skins [16,17]. Moreover, LPCS has been widely

used in industrial applications due to its outstanding advantages, such as its simple and portable equipment.

However, nozzle clogging has been the major challenge associated with all cold spray processes [18] and will become severer when particle velocity and temperature are increased. To eliminate this problem, a blended powder was used, in which larger or harder particles were added to the original powder [19,20]. To date, ceramic particles have been widely applied to deposit metal matrix composites (MMCs) such as AA 5056-SiC_p [21], Al-Al₂O₃ [14] and Cu-CNT-SiC [22]. Compared to the cold sprayed metals and alloys coatings, the presence of ceramic particles in MMCs can increase the plastic deformation of the metal matrix while simultaneously reduce the coating porosity, improve the hardness, wear- and corrosion- resistance [14,21–23]. Among the ceramic reinforced materials, SiC is the most commonly used in metallic-matrix composites (MMCs). The second one is Al₂O₃. However, when compared with SiC, Al₂O₃ is more stable and inert and has better corrosion and high-temperature resistance [24]. Moreover, the shot-peening effect has been especially applied to obtain dense coating by adding large particles into the feedstock powder. Wei et al. [25] added stainless steel powder which was in the range of 150–200 µm into the feedstock Ni powder and obtained fully dense Ni coating due to the enhanced shot-peening effect as compared with the conventional cold spray. Zhou et al. [26] used stainless steel 1Cr18 as shot-peening

* Corresponding author at: Key Laboratory of Nuclear Materials and Safety Assessment, Institute of Metal Research, Chinese Academy of Sciences, Shenyang 110016, China.

E-mail address: fcliu@imr.ac.cn (F. Liu).

particles with a size distribution from $\sim 125 \mu\text{m}$ to $\sim 300 \mu\text{m}$ and found that the coating was denser at the regions tamped by shot-peening particles than non-tamped regions.

Typically, the employed Al_2O_3 particles are in an angular morphology which will enhance the possibility to embed into the metal matrix. However, as observed in our previous work [27], the hard, angular Al_2O_3 particles would erode the nozzle wall and thus, shorten its service life, affect the nozzle operation and lead to variations in operating conditions and deposit quality. Besides, fragmenting of the brittle Al_2O_3 particles resulted from a collision in the powder jet also has been reported in [28,29]. However, Shockley et al. [30] found that the “critical” concentration of Al_2O_3 required to form an Al-Al $_2\text{O}_3$ composite layer with low wear rates and low friction was strongly dependent on the morphology of the Al_2O_3 particles, that is less spherical Al_2O_3 being needed compared to angular. Moreover, Shockley et al. [30] also found that significantly less spherical Al_2O_3 particles compared to angular ones were recovered at similar feedstock concentrations. Thus, using spherical Al_2O_3 particles instead of angular ones may be beneficial to reducing the clogging and erosion of the nozzle.

Cold sprayed Al-Al $_2\text{O}_3$ composite coatings have been intensively studied including the microstructural, tribological, mechanical and electrochemical properties [14,28–30]. The results revealed that the composite coatings exhibited lower porosity, typically $< 1\%$, and excellent wear and corrosion resistance compared with commercially pure (CP) Al coatings. Tao et al. [29] deposited Al and Al-Al $_2\text{O}_3$ composites and found that the composite coatings had lower porosity and better mechanical properties than CP Al coating. The polarization testing revealed that the corrosion current densities of the composite coatings were the same order as that of the CP Al coating. And SEM morphologies of the cold sprayed coatings after potentiodynamic polarization in 3.5 wt% NaCl solution showed no preferential corrosion occurred at the interface of Al and Al_2O_3 particles. Thus, the addition of Al_2O_3 has no passive effect on the anti-corrosion ability of the composite coatings when compared to that of the CP Al coating [29]. Based on these improved physical and mechanical advantages, ceramic reinforced aluminum-matrix composites (AMCs) have been a preferred choice for aircraft component reparation [31]. Sirvent et al. [32] deposited Al 2024 coating on the AA2024-T351 with low porosity and a good contact interface at the substrate and between particles using 500 °C and 350 °C deposition temperatures. Yang et al. [33] sprayed Al 2024-Al $_2\text{O}_3$ MMCs and then modified them with different passes of friction stir processing (FSP). The corrosion resistance of the cold sprayed AA2024/Al $_2\text{O}_3$ coatings could be significantly enhanced by low pass number FSP with the highest corrosion performance occurring at 2-pass FSP and the authors attributed this to the surface condition improvement after FSP [33]. With increased pass number, the negative effect of deteriorated interfaces of the inside coatings surpassed the positive effect of the improved surface condition and induced the unsatisfactory corrosion performance at 4-pass FSP [33]. However, to the best of the authors' knowledge, there are few studies that examined the corrosion behavior of low-pressure cold sprayed Al 2024-Al $_2\text{O}_3$ composite coatings, specially reinforced by spherical Al_2O_3 particles. Besides, 5XXX series aluminum alloys also have been widely applied in the aerospace industry as structural materials due to their excellent corrosion resistance, welding performance, and medium mechanical properties. The microstructure and corrosion behaviors of SiC $_p$ reinforced Al 5056 composite coating have been examined by Wang et al. [21,34]. Though the addition of SiC $_p$ particles yielded denser coatings, the inter-particle boundaries between Al 5056 matrix and SiC $_p$ particles and the cracks inside the large fractured SiC $_p$ particles provided passages for solution entering the deposits and accelerated the failure of the coatings. Despite the growing interest in cold spray deposited aluminum alloy coatings, however, there is a lack of comprehensive studies that have investigated the mechanical and corrosion properties of cold sprayed Al alloys coatings containing different precipitates.

The present paper aims to study the microstructural, mechanical and corrosion behavior of cold sprayed Al, Al 2024, and Al 5083

coatings and provide a reliable solution to the reparation of damaged AA2024-T3 applied in the aerospace industry. In order to eliminate the negative influence of Al_2O_3 addition to the largest extent, spherical Al_2O_3 particles are employed, based on the fact that significantly less spherical Al_2O_3 particles would emerge in the deposited coating compared to angular ones. According to our preliminary work and reference [33], the optimized Al_2O_3 content in the feedstock is set at 20% for the purpose to obtain relatively better mechanical and corrosion properties of the coating. Correspondingly, the coatings prepared with these composite powders were denoted as CP Al coating, Al 2024 coating, and Al 5083 coating, respectively. Furthermore, the deposition parameters such as gas pressure, powder feeding rate, gas preheating temperature, etc. have also been optimized according to the performance of the spray equipment.

2. Experiment

2.1. Feedstock materials and substrate

The nitrogen-atomized commercially pure (CP) Al, Al 2024, Al 5083 powder and the reinforcement Al_2O_3 particles were purchased from Shenyang Zhongke Corrosion Control Engineering Technology Co, Ltd., China, all of which were spherical in shape and ranged from 15 to 45 μm and 15 to 50 μm , respectively. The AA2024-T3 substrate was obtained from Dongguan J.Hone Metal Materials Co., Ltd., China, and its nominal composition was shown in Table 1. Prior to the spray process, the Al-based powder and Al_2O_3 particles were homogeneously mixed and oven-dried at 100 °C for 30 min and the substrate surface was sandblasted using 24 mesh silica sand under a pressure of 0.7–0.8 MPa, with the aim to obtain better bond strength. The measured roughness of the substrate is $\text{Ra} = 5.19 \pm 0.53$, a mean value of three measurements. A stylus-based surface roughness measurement instrument (Taylor Hobson, PGI 1240) was used to measure the substrate surface roughness with a measuring length of 5 mm.

2.2. Coating preparation

An in-house low-pressure cold spray system (as shown in Fig. 1S) mainly containing a set of spray equipment (DYMET 423#, Odninsk Center for Powder Spraying) and a semi-automatic X-Y's mobile platform, was employed to deposit the coatings. A convergent-divergent de Laval nozzle with $\Phi 2.4 \text{ mm}$ throat diameter, 120 mm divergent section length, and $\Phi 4.9 \text{ mm}$ exit diameter was used to accelerate the mixed powders. The N₂ was used as the carrier gas to accelerate the powder. During the deposition process, the compressed gas flowed through the nozzle throat and expanded to atmospheric pressure, which resulted in supersonic flow conditions. The feedstock powder mixed with the N₂ at the downstream flow and then got accelerated and finally deposited on the substrate. The spray parameters employed were listed in Table 2. The parameters were optimized prior to the final spraying process and we found that deposition efficiency (DE) typically increased with the increase of preheating temperature (200–600 °C) and gas pressure (0.6–0.8 MPa). When the N₂ was preheated at 600 °C, the maximum output of the equipment, the deposition efficiency increased significantly. Accordingly, regardless of the feedstock powders, the spraying parameters were kept the same for all the specimens. After that, the prepared coatings were kept in a drying cabinet (20 °C, 10% humidity) for at most 72 h before the testing.

Table 1
Chemical composition of AA 2024-T3 (wt%).

Si	Fe	Cu	Mn	Mg	Cr	Zn	Ti	Al
0.50	0.50	4.54	0.63	1.2	0.1	0.25	0.15	Balance

Table 2
LPSC process parameters of spraying powder.

Carrier gas	N ₂
Gas temperature	600 °C
Gas pressure	0.8 MPa
Powder feed rate	50 g/min
Scan speed	30 mm/s
Spray angle	90°
Standoff distance	12 mm
Number of passes	3

2.3. Microstructural, morphological and mechanical characterization

The morphologies and chemical compositions of the powders, as well as the composite coatings, were analyzed using an XL 30 type field emission scanning electron microscope (Philips, Holland) which is equipped with the EDAX analysis hardware to analyze the surface energy spectra. To get better conductivity on the surface, Au was sprayed on the samples prior to SEM observation. Thus, the detected Au content in EDAX spectra analysis was excluded.

After the spraying process, the specimens were prepared for the metallographic analysis following the standard ASTM E1920 [35]. The metallographic photographs were obtained by the optical microscopy (OM) equipment (Zeiss Microscopy A2.m, Oberkochen, Germany) equipped with DICRA and polarizer. The metallographic characterization of coatings was conducted on the metallographic photographs. The porosity assessment was conducted using micrographs with 500 x magnification, in grayscale, converted to 8 bits through the threshold as specified by standard ASTM E2109 [36]. To distinguish the particles and the coating/substrate interfaces, the samples for SEM observation were etched in a solution consisting of 1.0 vol%HF, 2.5 vol%HNO₃, 1.5 vol%HCl and 95 vol%H₂O for 20 s.

The deposition efficiency (DE) was determined by the ratio of increase in the weight of the substrate to the drop in sprayed powder weight in the powder feeder. Three measurements were calculated for each coating. Microhardness measurements were performed on mounted samples using a conventional Vickers hardness tester (FUTURE-TECH, FM-700, Japan) with a 100 g load and a dwell time of 15 s. To obtain more reliable results, the test points were chosen on aluminum-rich area to avoid the influence of Al₂O₃ particles. The final value is the average value of ten measurements.

The bonding strength of the coating was measured according to the standard ASTM C633 using a Z-axis stud pull machine [37]. Firstly, a coating of approximately 0.15–0.2 mm in thickness was deposited on one end face of the AA2024-T3 cylinder slug. Then the coated surface was immersed in sulfuric acid-potassium dichromate solution for 1 min to clean the surface and then washed by flowing water and finally scrubbed with acetone and dried. After that, the coated surface and the other end surface were glued to the grit-blasted surface of two cylinder spindles with a diameter of 25.4 mm. After the adhesive was cured at 100 °C for 240 min, a uniaxial load was applied on the spindles by an electronic tension testing machine (Zwick-z150, Germany) at a cross-head speed of 0.5 mm/min to break the specimen. The average and standard deviation of measurements per set of five samples were calculated.

A multifunction X-ray diffractometer (Smart Lab, Rigaku™, Japan) utilizing CuK α as the radiation target at a working voltage of 20 kV and current of 30 mA, was used for the measurements of compressive residual stress. The measurement was taken by the X-ray diffraction sin²Ψ method [38]. The residual stress calculations of the specimen were done by X-ray diffraction sin²Ψ method. Where “Ψ” is the angle between the normal to the surface and the normal to the diffraction plane (<311>). The residual stresses were measured in the σ_x direction [38].

XPS (ESCALAB, 250, USA) with Al K α excitation ($h\nu = 1486.6$ eV) was adopted to analyze the component of the original oxide layer. The measured coating surfaces for XPS were well polished and cleaned by

distilled water. The XPS tests were conducted at about 0.1 nm/s sputtering rate with argon ions (2 mA, 3 kV). The test area of XPS is a roughly circular spot of 0.5 mm in diameter. The standard carbon contamination (284.6 eV) was adopted for the calibration of binding energy. The software of XPSPEAK 4.1 was used for the XPS data processing.

2.4. Electrochemical measurements

All the electrochemical measurements were performed using a 273A electrochemical workstation from EG&G (USA) with a conventional three-electrode cell under room temperature (25 ± 1 °C). The cold sprayed coating sample was used as the working electrode in 12.56 cm² exposed area, a Pt grid of 2 × 2 cm² as the counter electrode and the saturated calomel electrode (SCE) as the reference electrode. The corrosive electrolyte is non-deaerated and quiescent 3.5% NaCl aqueous solution (pH 6.5–7.5, humidity 40–60%). Prior to each test, the sample surface was ground to 1000# by silicon carbide abrasive paper and for clear observation of corroded region, the cyclic polarization samples were further finely polished, then ultrasonic cleaned in acetone and finally dried in air. The structure schematic diagram of the electrochemical cell for EIS measurement is shown in Fig. 3S.

The corrosion resistance of the coatings in 3.5% NaCl solution was evaluated in the electrolyte by open circuit potential (E_{OCP}) measurements, cyclic polarization (CP) and electrochemical impedance spectroscopy (EIS). Cyclic polarization measurements were performed after 6 h of immersion with a rate of 1 mV/s, beginning at -0.15 V/E_{OCP}. The reversal scan started when the anodic current density reached the pre-selected value of 1 × 10⁻³ A/cm². Finally, the scan ended at -0.15 V/E_{OCP}. The open circuit potential (E_{OCP}) and electrochemical impedance spectroscopy (EIS) were measured using the same samples in the following order: (1) E_{OCP}, (2) EIS after the E_{OCP} was stable. The area of the working electrode was 12.56 cm². The immersion time for the measurements was set as 720 h. EIS measurements were carried out in a frequency range from 100 kHz to 10 mHz, by implying a sinusoidal perturbation of 10 mV at E_{OCP}. Totally 30 logarithmically distributed points were collected using the PowerSuite® program and the Electrical Equivalent Circuit (EEC) was fitted using Zview® program in order to quantitatively analyzed the EIS results.

A commercial SVET system from Applicable Electronics Inc. (USA), controlled by the Science Wares ASET 2.0 software, was used. The Pt–Ir probe (Microprobe Inc.) was platinized to form a small, 30 μm diameter, ball of platinum black at the tip. The frequency of probe vibration in the perpendicular direction to the sample surface was 325 Hz. The measurements were taken at open circuit potential. The time of acquisition for each SVET data point was 0.6 s. The current densities were detected on 100 μm above the sample surface within an area of approximately 2.5 × 2.5 mm² for the couplings. SVET allows the identification of anodic zones (positive currents) and cathodic zones (negative currents) above the corroding surface in the aggressive medium.

3. Results and discussion

3.1. As-received powders

Fig. 1 shows the SEM images of the as-atomized Al, Al 2024 powder, Al 5083 and Al₂O₃ powders. All the particles present a spherical shape and are surrounded by micro-satellite particles (< 5 μm). Table 3 shows the composition of aluminum powders used for producing cold spray coatings. Fig. 2 shows the backscattered electron (BSE) images of as-polished cross-sections of Al, Al 2024, and Al 5083 powder. Fig. 2(a) shows the BSE image of the Al powder, which exhibits a uniform microstructure without obvious intermetallic phase. Besides, a small number of pores could be found in the Al coating. For the Al 2024 powder, there exist two types (see in Fig. 2(b) and (c)) of particles

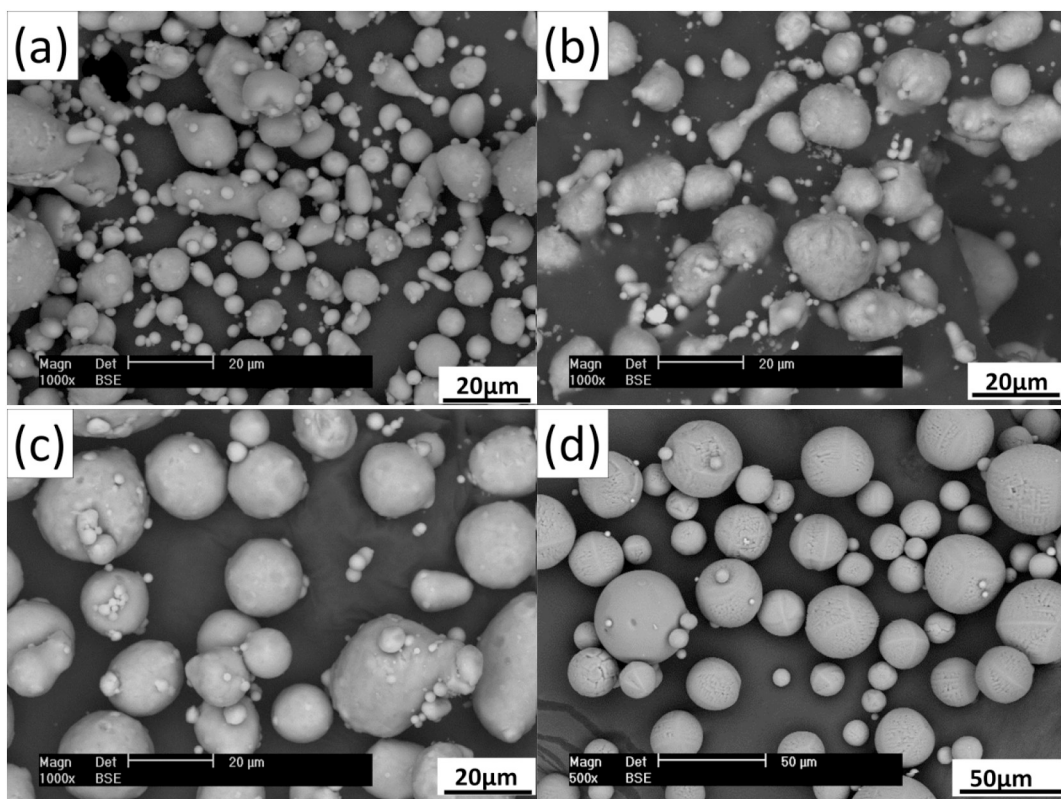


Fig. 1. SEM images of the powders: (a) pure Al, (b) Al 2024, (c) Al 5083 and (d) Al_2O_3 .

according to the internal microstructure features. Type I particles, as shown in Fig. 2(b), exhibit a cellular-like dendritic solidification microstructure. According to the EDAX analysis in Fig. 2S(a) (Supplementary data), the brighter and whiter lines in type I particles are intermetallic phases which are rich in Cu. The inert gas atomization is often employed to produce feedstock powders with fine particle sizes (10–40 μm) for cold spray, of which a dendritic microstructure is a common feature due to the solute segregation effect. The main reason leading to solute segregation is the extremely high cooling rates which are expected to be in the range of 10^4 – 10^5 K/s [39]. Type II particles, as shown in Fig. 2(c), have a more uniform microstructure without pronounced precipitation in the Al matrix and mainly contain Al and Mg, based on the EDAX analysis in Fig. 2S(b). The composition difference between type I and type II particles may be attributed to the heterogeneous composition distribution of Cu and Mg in the liquid aluminum on the microscopic scale. The morphology of Al 5083 particles is displayed in Fig. 2(d). It can be observed that a few pores are trapped and bright intermetallic phases are scatteredly distributed inside the particle, which are rich in Mg according to the EDAX measurement. Wei et al. also observed similar microstructures for pure Al, AA2219, and AA 6061 powders [40]. Besides, the dendritic microstructure with clearly visible dendrite boundaries (bright precipitates) indicating the formation of intermetallic was reported in [41,42]. The different microstructures of Al 2024 and Al 5083 powders can be attributed to the

lower solid solubility of Cu in α -Al compared with Mg. As a result, excessive Cu was precipitated during the solidification process.

3.2. Microstructures and mechanical properties of the cold spray deposited coatings

3.2.1. Microstructural features

Fig. 3 depicts the dense microstructure without obvious through-thickness pores/cracks of CP Al, Al 2024, and Al 5083 coatings, respectively. Since there is almost no obvious precipitate in the CP Al particle, the cross-sectional morphology of CP Al coating depicted in Fig. 3(a) shows a uniform microstructure with very few Al_2O_3 particles trapped in the coating. Fig. 3(b) reveals that the Al 2024 coating consists of the type I and type II particles, as well as the Al_2O_3 particles. Besides, some pores could be seen inside the coating, which are not interconnected with each other. Fig. 3(c) shows that the Al 5083 coating also possesses a uniform microstructure with very few Al_2O_3 particles trapped in the coating. Fig. 3(d), (e), (f) are the morphologies of coating/substrate interfaces at higher magnification. No obvious defects such as pores and cracks can be seen on the interfaces (marked by yellow arrows) while some fractured Al_2O_3 particles attached at the coating/substrate interface (see Fig. 3(a), (e), (h)). However, the interface of Al 2024 coating is not clear and this may be attributed to their similar chemical composition. The precipitate particles are not

Table 3

Composition of aluminum powders used for producing cold spray coatings (wt%).

Identifier	Al	Cr	Cu	Fe	Mg	Mn	Si	Zn	O	Others
CP Al	Bal.	–	0.002	0.090	–	–	0.046	–	0.022	–
Al 2024	Bal.	–	3.952	0.185	1.320	0.450	0.087	0.25	0.008	< 0.05
Al 5083	Bal.	0.19	0.044	0.016	4.71	0.70	0.074	0.056	0.008	

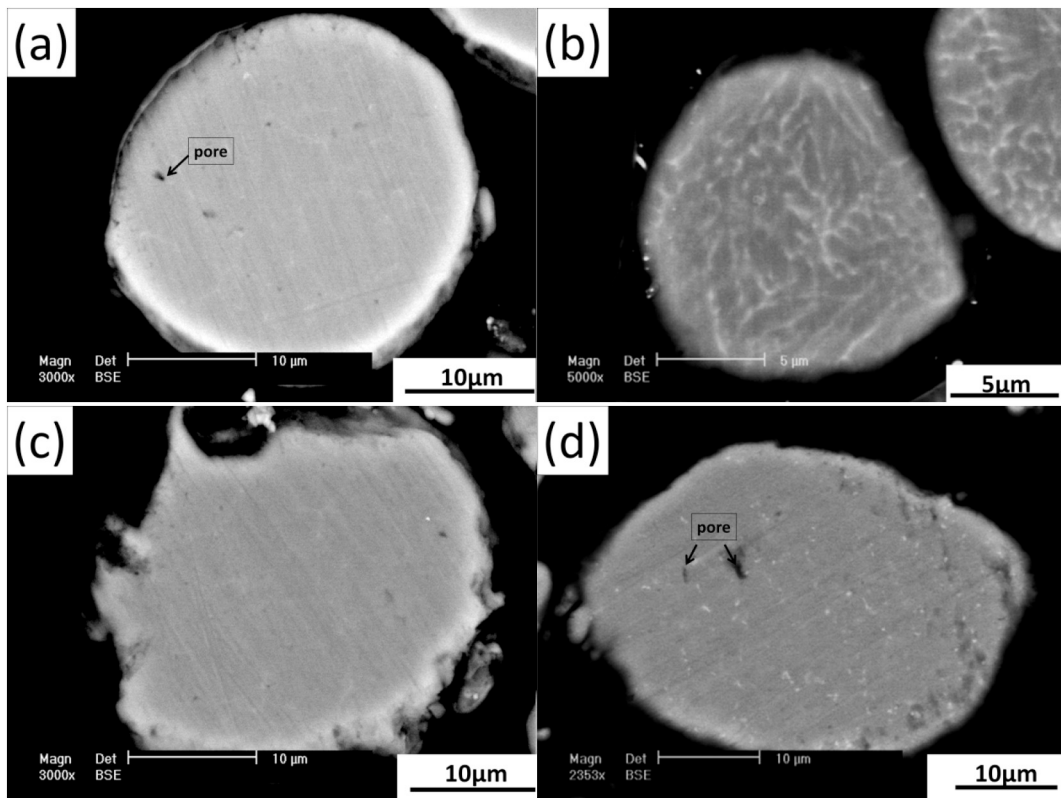


Fig. 2. BSE images of cross-sectional of (a) pure Al, (b) Al 2024 type I particle, (c) Al 2024 type II particle, and (d) Al 5083.

observed due to the relatively low magnification. Similarly to the Al 2024 coating, a small number of unconnected pores could be found in the coating.

Besides, it is obvious that the proportion of Al_2O_3 in the three coatings is much lower than that in the mixed feedstock powder. The rebound of the hard Al_2O_3 particles was observed elsewhere [27,29,30]. Shockley et al. [30] found that the recovery of spherical Al_2O_3 particles in the CP Al coating was lower compared to the angular ones and they attributed this phenomenon to the more stringent criteria for embedding spherical particles. Wei et al. [43] found in their studies that although the velocity of the 1Cr18 stainless steel particles was well lower than the critical velocity, the particles were still observed in the coating cross section. The authors ascribed this phenomenon to the penetration when mechanically mixed hard and soft metallic particles were used to prepare composite coatings [43]. The lower recovery of spherical Al_2O_3 compared to the angular morphology can be partly explained by [44] which studied the embedding behavior of hard spherical and angular particles in ductile substrates by modeling and experimental work. In both cases, the embedding of particles during impact could be prevented sufficiently by elastic rebound forces unless certain criteria were met. For angular particles, the flat sides and sharp corners ensured the directions of the normal and tangential components of elastic rebound forces to be constant, and once the static friction forces between the particles and substrates reached the criteria, the particles will embed according to Getu et al. [44]. In the case of spherical particles, higher elastic rebound forces normal to the impact direction are required due to the constant curvature of the particles, and to embed successfully, the particles must impact to a depth greater than its radius and be enveloped by material [44]. Furthermore, the authors also predicted that spherical particles were not able to embed at impact angles perfectly normal to the substrate, as the elastic rebound forces were always higher than the retaining friction forces.

Moreover, all the coatings show dense microstructures without interconnected pores. To calculate the porosity of the coatings, ten

micrographs at a magnification of 1000 X for each coating were used to measure the porosity. The porosity of CP Al coating, Al 2024 coating, and Al 5083 coating is $1.46 \pm 0.06\%$, $1.66 \pm 0.16\%$, and $1.50 \pm 0.17\%$, respectively. The dense structures enable the coatings to shield the substrate against corrosion medium effectively. Moreover, compared with the angular Al_2O_3 reinforced composite coatings [29,33], no fractured spherical Al_2O_3 particles are observed inside the coating, which is beneficial for the decrease of porosity.

Fig. 3(g-i) showed the etched cross-sectional microstructure of the cold sprayed coatings. Prolonged particles perpendicular to the impact direction could be observed for all the coatings, as indicated by the “horizontal” interfaces. The particle morphology change here confirmed the occurrence of plastic deformation during the deposition process. According to [25,40,43,45], the particle deformation is mainly due to the in-situ shot peening effect of the hard spherical Al_2O_3 particles.

Meanwhile, the deposition efficiencies (DE) of the Al, Al 2024, and Al 5083 coatings are $2.69 \pm 0.28\%$, $3.33 \pm 0.24\%$, and $2.93 \pm 0.19\%$, respectively. Meanwhile, the ratio of Al_2O_3 in the coating is very low and difficult to calculate, so the DE of Al_2O_3 particles was not presented in this work. Moreover, the spraying parameters were set the same for the three coatings, thus, the thickness of the coating can directly signify the DE qualitatively. As depicted in Fig. 3, the thicknesses of the three coatings are within the range of 90–100 μm , 120–140 μm , and 160–170 μm , which agrees with the DE results.

3.2.2. Cohesive strength measurements

The cohesive strengths to the substrate for the three coatings are shown in Fig. 4(a). The digital photos of the failed samples are shown in Fig. 4(b). It can be observed that the fracture partly occurred inside the coating for Al and Al 2024 coating samples. Some of the Al 5083 coating samples fractured inside the coating and the others on the coating/substrate interface. Thus it is more accurate to call it cohesive

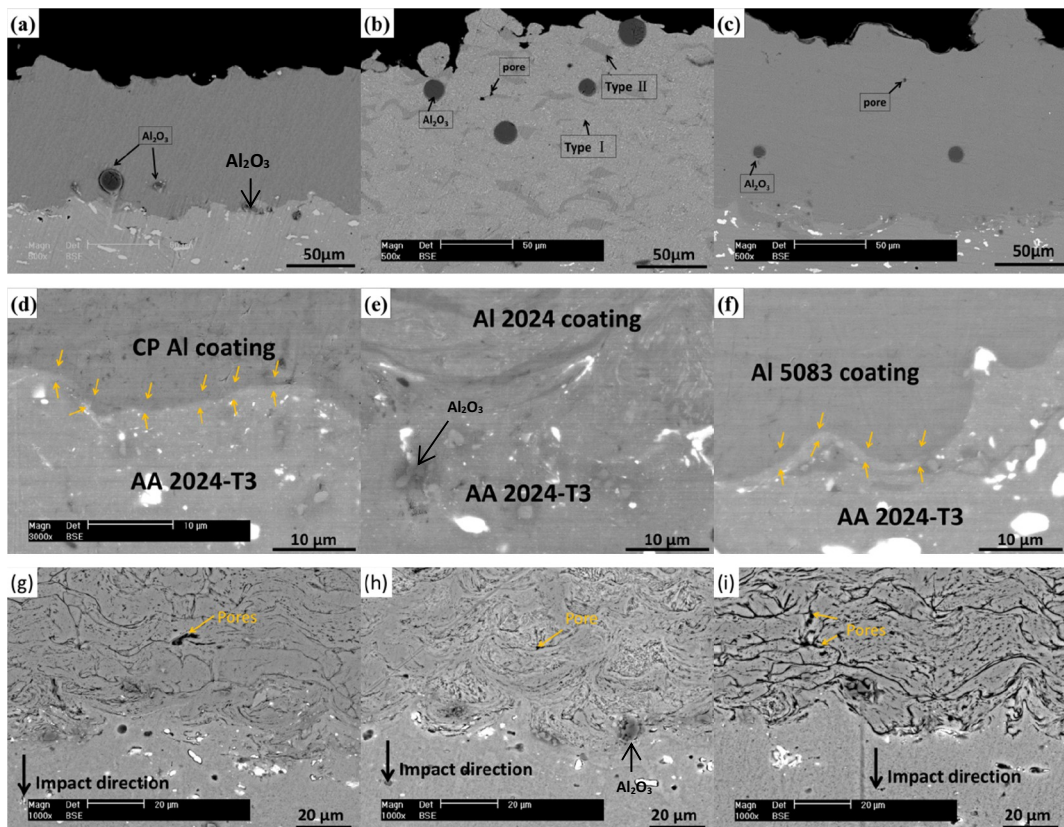


Fig. 3. Cross-sectional microstructures of (a) Al, (b) Al 2024, and (c) Al 5083 coatings. (d), (e), and (f) are the higher magnification SEM images at the coating/substrate interface, (g), (h), (i) are the etched SEM images corresponding to (a), (b), (c), respectively.

strength. The average cohesive strengths of CP Al coating, Al 2024 coating and Al 5083 are 46 ± 6 , 50 ± 7 and 51 ± 6 MPa, respectively. Fig. 3 clearly shows the coating/substrate interfaces of the coatings. No micro-cracks or pores can be traced at the coating/substrate interfaces, indicating the excellent peening effect of Al₂O₃ particles, which is beneficial for the deeper penetration of the sprayed Al-based particles into the AA2024-T3 substrate. Based on the analysis above, an illustration of the deposition process of spherical Al₂O₃ particles reinforced cold spray is displayed in Fig. 5. Moreover, the measured cohesive strength values are higher than those of the conventional angular Al₂O₃ particles reinforced Al-Al₂O₃ coatings [14,29] and the Cu-Al₂O₃ coating [46].

3.2.3. Microhardness measurements

The microhardness measurements across the coatings and substrates are shown in Fig. 6. The average hardness value of CP Al coating (~ 57 HV_{0.1}) is about half of that of the Al 2024 coating (~ 115 HV_{0.1}) and the Al 5083 coating exhibits the highest hardness (~ 132 HV_{0.1}). The elasticity, plasticity, strength, and toughness, wear resistance as well as a series of different physical and mechanical properties of a certain material can be generally presented in terms of hardness; therefore, hardness is an important parameter for the evaluation of materials [47]. From this perspective, the Al 5083 coating is more bearable to harsh service conditions. By comparison, Yang et al. deposited AA 2024-Al₂O₃ composite coatings through cold spray using helium as the accelerating gas at the inlet pressure of 0.8 MPa and temperature of 500 °C, and the measured microhardness is 125 HV_{0.1} [33]. Silva et al. [14] deposited CP Al coating and angular Al₂O₃ particles reinforced Al composite coating using N₂ as streaming gas with a pressure of 25 bar and a temperature of 350 °C. The microhardness values of the two coatings are 51 ± 3 HV_{0.1} and 65 ± 5 HV_{0.1} respectively. It seems that the microhardness values of the coatings in this

work are comparable to those of the angular Al₂O₃ particles reinforced coatings. Thus, though the trapped spherical Al₂O₃ particles in coatings are significantly lower than the angular ones, similar work hardening effect could be induced on the Al-based particles due to the shot peening effect. Microhardness of cold-sprayed metallic coatings is dependent mainly on coating porosity and microstructure changes during the deposition process including dislocation multiplication (work hardening) and inter-particle recrystallization (grain refinement strengthening) [48]. As shown in Fig. 3(g-i), the Al-based particles went through severe plastic deformation during the spraying process by the in-situ shot peening effect, which resulted in the low porosity and high hardness of the coating. Similar results can be observed in [25,40,43,45], which showed enhanced microhardness by the in-situ shot peening effect.

3.2.4. Residual stress measurements

Fig. 7 depicts the residual stresses variations of the three coatings on the surface of the coatings. All the coatings show negative residual stresses values, namely compressive residual stress (CRS) due to the peening effect by high velocity particle impact [48,49], among which the Al 5083 coating shows the highest values (57.98 ± 1.21 MPa) and the CP Al coating shows the lowest ones (32.14 ± 1.25 MPa). Upon impacting on the substrate or the deposited layer, the high-speed Al alloy particles were lengthened along the surface (Fig. 3(g-i)), which caused strong plastic deformation, but the substrate impeded the change, resulting in compressive stress in the coatings [50]. The variation in residual stresses can be attributed to the variations of material content according to Spencer et al. [51]. The authors compared the residual stress profile of cold sprayed CP Al, 7075 Al and 6061 Al coatings with the same conditions and found the residual stress profiles depended more on the alloy content, i.e. intrinsic resistance to plastic deformation, than on the processing conditions, and this result was well

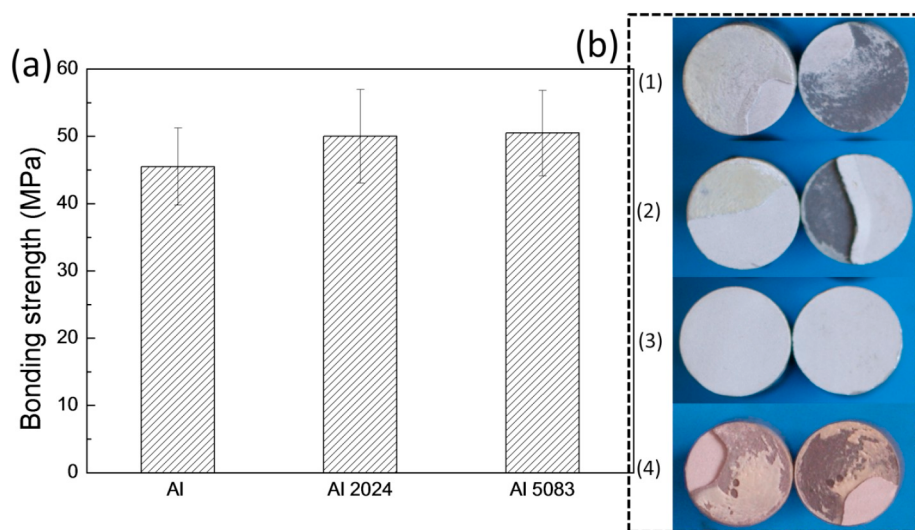


Fig. 4. Cohesive strengths of the coatings (a) and digital photos of the failed samples (b), where (1) for CP Al coating, (2) for Al 2024 and (3), (4) for Al 5083coating.

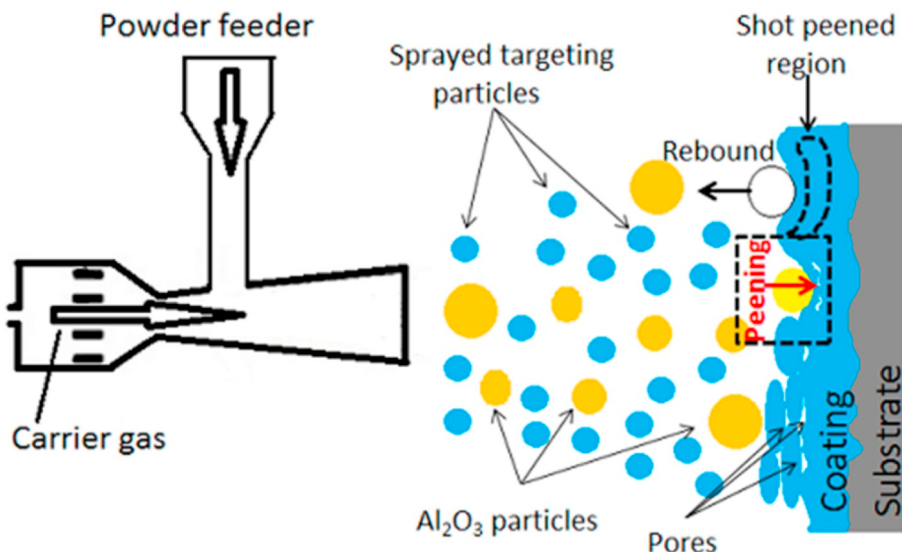


Fig. 5. A schematic illustration of spherical Al_2O_3 particles reinforced the cold spray process.

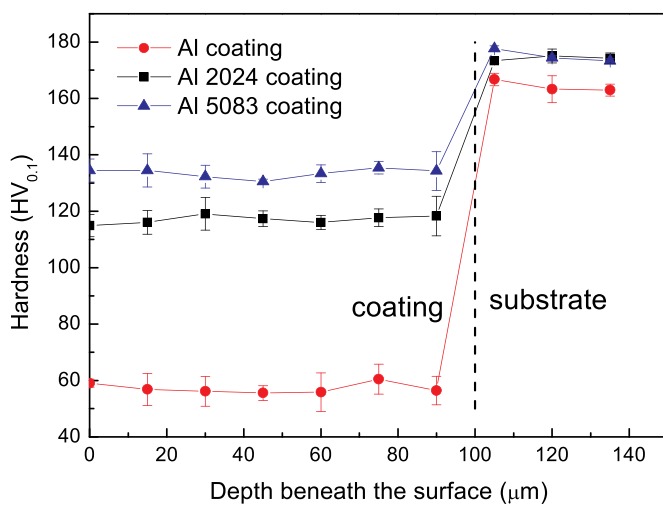


Fig. 6. The microhardness distribution along the coating thickness.

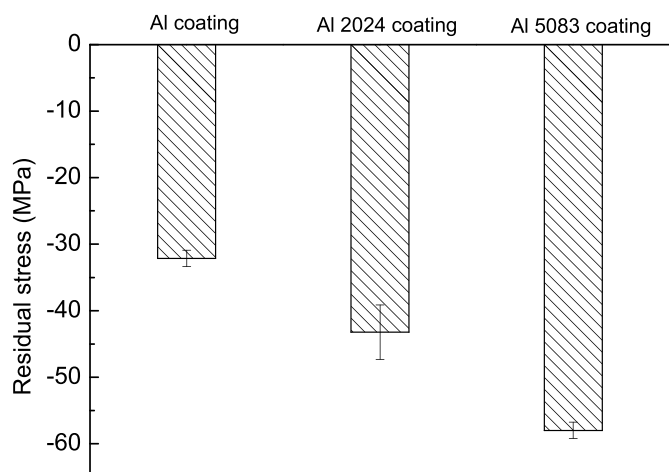


Fig. 7. Residual stress measurements of the coatings on the top layer of the coating.

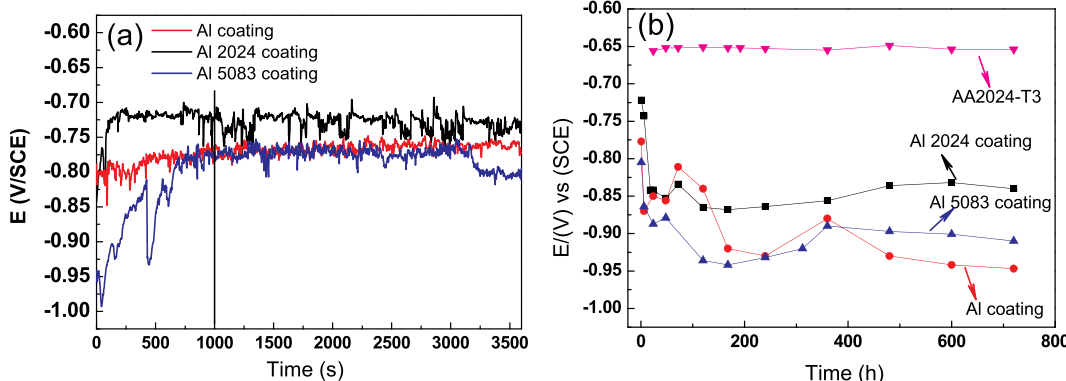


Fig. 8. Open circuit potential vs. time for the cold sprayed coatings measured in 3.5 wt% NaCl solution: (a) for the initial immersion stage, (b) for an immersion time of 720 h.

explained using a simple model that incorporated the effect of peening stresses in the cold spray process [51]. Meanwhile, Oladijo et al. [52] reported compressive stresses could render better wear resistance while tensile stress coatings led to weak performance. Besides, according to the previous literature [25,53], CRS is beneficial for corrosion resistance by closing the micro-cracks that would be directly perpendicular to the coating surface.

Briefly, by mixing the spherical Al_2O_3 particles into feedstock, dense Al-based coatings without through-thickness pores were successfully achieved by cold spraying due to the in-situ peening effect by the Al_2O_3 particles. Moreover, Al 5083 coating exhibits the highest cohesive strength, residual stress, microhardness and relatively low porosity among the three coatings.

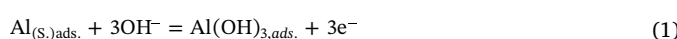
3.3. Corrosion test

3.3.1. Open circuit potential and cyclic polarization test

The E_{OCP} evolution of the coatings during the first hour of in 3.5% NaCl solution is depicted in Fig. 8(a). The E_{OCP} curves of cold sprayed Al-based coatings exhibit a similar variation tendency consisting of two stages. In the first stage (0–1000 s), E_{OCP} values increased dramatically, implying that surface passivation occurred as a result of formation of a more protective oxide film on the substrate surface when exposed to solution [14,54]. Then, the E_{OCP} gradually reached a plateau, indicating a dynamic balance between the formation and dissolution of the aluminum oxide [40]. The stabilized E_{OCP} values for CP Al, Al 2024 and Al 5083 coatings are around -0.76 V, -0.72 V, and -0.77 V vs. SCE, respectively.

Besides, the coatings and substrate were also examined by E_{OCP} measurements for 720 h, as shown in Fig. 8(b). During the first 24 h, all the E_{OCP} values of the coatings showed a rapid decreasing trend, which was associated with the dissolution of oxides from some weak points of the oxide. A similar result was found by Silva et al. on the cold sprayed Al coating [14]. Afterwards, the E_{OCP} values oscillated and finally stabilized at different potentials depending on the materials: CP Al (-0.95 V/SCE), Al 2024 (-0.85 V/SCE) and Al 5083 (-0.89 V/SCE). The oscillations of potential were caused by the formation and re-passivation of pits on aluminum surface [55]. However, the E_{OCP} values of AA 2024-T3 substrate stabilized around -0.65 V/SCE throughout the whole testing time.

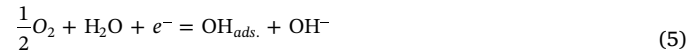
It is well known that Al-based alloys and coatings are susceptible to pitting corrosion, especially in the medium that contains Cl^- . It is well recognized that a thin oxide layer will form on aluminum surface when exposed to a NaCl solution. The following two reactions were involved on Al surface [56,57]:



In 3.5% NaCl solution, pitting took place due to the attacking of Cl^- on the surface oxide layer which turned atom Al into Al^{3+} because of the reactions:



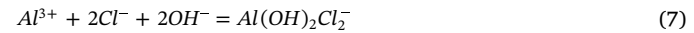
Besides forming aluminum chloride complex, a cathodic reaction also took place:



The hydroxide species adsorbed on the aluminum surface were further formed as follows:



In addition, the Cl^- can also react with Al^{3+} to form an oxychloride compound, as shown in Eq. (7). This increases the anodic dissolution, [56,57]:



In order to fully evaluate the corrosion behavior of the cold sprayed coatings, cyclic polarization measurement was adopted to get detailed information on E_{corr} , I_{corr} , E_{pit} , E_{rp} , etc. The measurements were conducted after the samples were immersed in a 3.5% NaCl solution for 6 h. The E_{OCP} values measured prior to the CP measurements were around -0.88 , -0.74 , and 0.86 V/SCE for the CP Al, Al 2024, and Al 5083 coatings, respectively. The typical cyclic polarization curves for

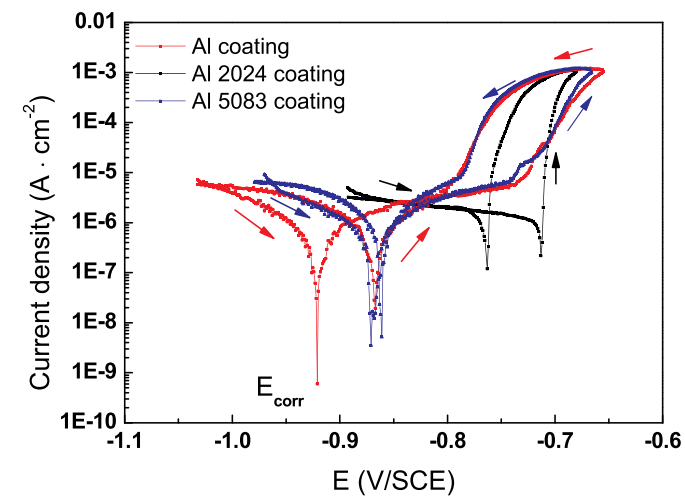


Fig. 9. Cyclic polarization of coated sample measured in 3.5 wt% NaCl solution at 1 mV/s, after 6 h of immersion.

all coatings are shown in Fig. 9. The solid arrows next to the forward and the reverse anodic branches indicate potential scan directions. On the forward scanning, the corrosion currents of Al and Al 5083 coatings decreased rapidly with the increase of potential, and reached the minimum at their E_{corr} respectively and then the current increased slowly with the increase of potential until a certain critical potential, known as the pitting potential E_{pit} , where a sharp increase in anodic current occurred due to the breakdown of passive film and the initiation of pitting corrosion [58,59]. However, the corrosion current of Al 2024 coating decreased at a relatively low rate with the increase of potential until the E_{corr} . After that, the current showed a sharp increase immediately. Typically, higher pitting potential means better resistance to pitting corrosion and thus, E_{pit} may be a good choice to indicate the corrosion resistance [60]. However, if the location of E_{pit} is not far above the E_{corr} , for example, Al alloys in chloride-containing solution, small increases of potential would cause pitting initiation. Once pitting occurred, despite the fact that the E_{corr} is lower than E_{pit} and new pitting will not occur, the existing pitting would continue to develop. Thus, under this circumstance, E_{pit} is not a proper parameter to predict the corrosion resistance. According to Kiourtsidis's work [61], the difference between corrosion potential (E_{corr}) and pitting potential (E_{pit}) may be a better guide to corrosion resistance. Smaller ($E_{pit} - E_{corr}$) indicates higher susceptibility to pitting [59,61].

On the reverse scan, all the coatings showed a positive hysteresis, indicating the further development of pitting. According to [62], if the reversed anodic curve is shifted to lower currents (negative hysteresis), or the reversed curve essentially retraces the forward curve (neutral hysteresis), pitting corrosion would not get further developed. In contrast, if the reverse anodic curve is shifted to higher currents than the forward curve, (positive-hysteresis), further pitting propagation is expected. As the potential continued to decrease, the reversed curve intersected the forward scan at the repassivation potential E_{rp} (or protection potential) under which pits would get repassivated, i.e., the existing pits will not continue to grow when $E < E_{rp}$.

Table 4 shows the average corrosion parameter values for the three coatings, obtained from three cyclic polarization curves, respectively. It can be seen that the CP Al and Al 5083 coatings show similar and relatively lower I_{corr} while Al 2024 coating shows significantly higher I_{corr} than the others, which means corrosion reactions on Al 2024 coating are severer than the CP Al and Al 5083 coatings. As mentioned above, a better guide to corrosion resistance is the difference between the pitting potential and the corrosion potential: the larger this difference, the more difficult it is for pitting to occur [59,61]. Analysis of the corrosion parameters ($E_{pit} - E_{corr}$) indicates that Al 2024 coating is most susceptible to pitting while the other two coatings show similar but lower pitting susceptibility. Furthermore, the differences in ($E_{rp} - E_{corr}$) values suggest the ability to repassivation in the following order: Al 2024 < Al 5083 < CP Al coating.

To further assure the corrosion behavior of the cold sprayed coatings, the tested samples after cyclic polarization were examined, as shown in Fig. 10. Fig. 10(a) reveals that the pitting site on the surface of CP Al coating is large and deep, with an irregular shape. One spherical Al_2O_3 particle is located at the edge of the pit and no preferred dissolution of Al matrix is observed on the Al-Al₂O₃ interface, which suggests that galvanic cell was not formed between the Al matrix and the Al_2O_3 particle. Besides, a layer of corrosion products had been

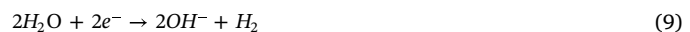
formed on the matrix which may partially isolate the coating from the electrolyte. As shown in Fig. 10(b), a large number of shallow pits are randomly distributed on the Al 2024 coating surface. The inserted figure with higher magnification reveals that the shallow pits were mainly formed around the bright Cu-rich precipitates, which is an indication of the galvanic corrosion between the cathodic Cu-rich precipitates and the adjacent anodic Al matrix. Fig. 10(c) shows that the pits on the Al 5083 coating are smaller in depth and size compared with those in the CP Al coating. The related EDAX results of pit bottom reveal the enrichment of silicon and the absence of Mg (see Fig. 4S). Also, some small pits with an irregular shape (2–3 μm , arrowed) are observed on the surface which is believed to originate from the anodic dissolution of the Mg-rich precipitates (such as Al_3Mg_2 and Mg_2Si [63]). The Mg-rich precipitates inside the Al 5083 particles usually act as anodes to the Al matrix. The related reactions produce dense hydroxide deposits such as $\text{Mg}(\text{OH})_2$, thus preventing the formation of deep pits, as propounded by Ezuber et al. [23] and Trueba et al. [64]. Therefore, with the accumulation of corrosion products, the corrosion resistance of Al 5083 coating may increase gradually by decreasing the exposed area to 3.5% NaCl electrolyte of the coating.

3.3.2. Scanning vibrating electrode technique

The SVET maps obtained for the three different coatings by the beginning of exposure and after 24 h in 3.5% NaCl solution, as well as the optical image of the respective surfaces by the end of exposure are depicted in Figs. 11–13.

At the initial stage of immersion (1 h), only one small pit has formed on the CP Al coating surface and later the anodic peak (red-colored region) experienced very little decline while the corroded zone had increased slightly up to the end of immersion (24 h), as shown in Fig. 11(a–c). Besides, the cathodic activity (blue color) spread over the remaining surface throughout the whole immersion time. Furthermore, the optical photographs (Fig. 11(d)) revealed that the bright background CP Al coating still could be observed and small darkened pits were evenly distributed on the surface after immersed for 24 h.

Three anodic peaks were observed on the SVET map of Al 2024 coating, one of which showed the highest peak value of $80 \mu\text{A}\cdot\text{cm}^{-2}$ after 1 h (Fig. 12(a)), indicating the high activity of the coating in 3.5% NaCl solution. 6 h later, the highest peak decreased to $70 \mu\text{A}\cdot\text{cm}^{-2}$ meanwhile some new small pits had formed (Fig. 12(b)). A large number of anodic zones and some noticeable cathodic zones emerged after 24 h of immersion (Fig. 12(c)), suggesting that both the anodic and cathodic reactions had become more active at that time. Fig. 12(d) showed that the darkened area, as an indication of corrosion, had spread over the whole coating surface. Moreover, three bubbles were found on the surface which implied that hydrogen reduction reactions still occurred even after long immersion times. Considering that in Al-Mg-Cu alloys, Cu usually acts as cathode and Mg acts as anodes and is more preferential to dissolve, thus the following reactions may account for the generation of hydrogen:



The number of anodic and cathodic peaks on the surface of the Al 5083 coating was much larger than those of previous coatings, as shown in Fig. 13(a–c). Meanwhile, the anodic peak values were under

Table 4

Average characteristic potentials (V vs. SCE) of the coatings from cyclic polarization scan after immersed in 3.5 wt% NaCl solution for 6 h. Each of the values is an average of three sets of data.

Coatings	I_{corr} ($\mu\text{A}/\text{cm}^2$)	E_{corr} (V/SCE)	E_{pit} (V/SCE)	E_{rp} (V/SCE)	$E_{pit} - E_{corr}$ (V)	$E_{rp} - E_{corr}$ (V)
Al	0.5 ± 0.1	-0.88 ± 0.04	-0.74 ± 0.02	-0.78 ± 0.03	0.15 ± 0.03	0.10 ± 0.03
Al 2024	3.2 ± 2.1	-0.71 ± 0.01	-0.71 ± 0.01	-0.76 ± 0.01	0	-0.05 ± 0.01
Al 5083	0.6 ± 0.2	-0.87 ± 0.01	-0.73 ± 0.01	-0.84 ± 0.01	0.15 ± 0.03	0.03 ± 0.01

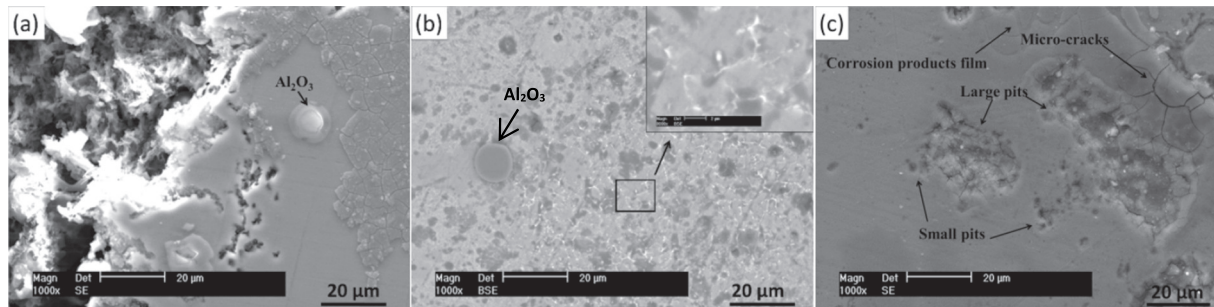


Fig. 10. Surface morphology of the cold sprayed coatings after CP corrosion test; (a) Al coating, (b) Al 2024coating, and (c) Al 5083 coating.

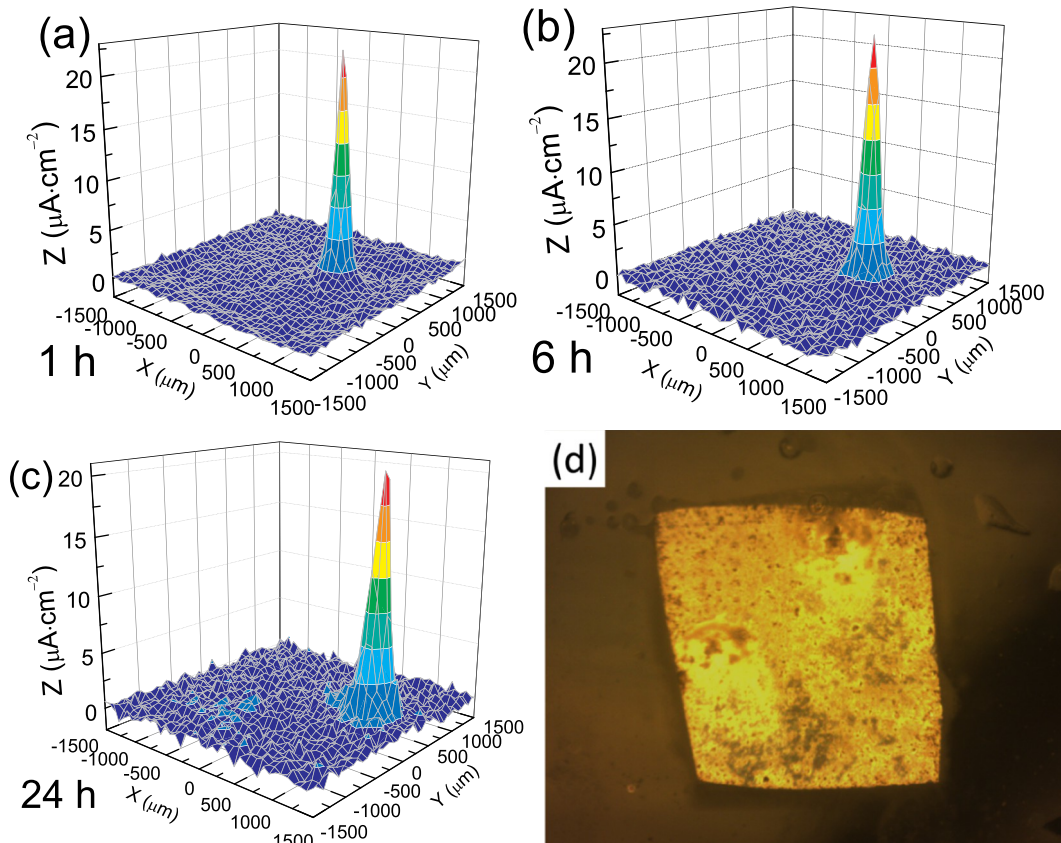


Fig. 11. SVET maps of Al coating by the beginning of exposure and after 24 h in 3.5% NaCl solution, as well as the optical image of the test surface. (For interpretation of the references to color in this figure, the reader is referred to the web version of this article.)

$10 \mu\text{A}\cdot\text{cm}^{-2}$ and showed a decreasing trend with increased immersion time. However, the cathodic peak values showed an opposite trend. The optical image (Fig. 13(d)) revealed that small darkened corrosion sites and several large corroded areas were distributed over the whole bright coating matrix.

Besides, the performances of the coatings were compared in Fig. 14 by plotting together the average anodic and cathodic current densities. These average current densities can be calculated by the following equation,

$$j_{an/cat}^{map \ average} = \frac{\sum_{n=1}^N j_{n(an/cat)}}{N} \quad (10)$$

where $j_{an/cat}^{map \ average}$ represents average anodic (or cathodic) current density of the measured area, $j_{n(an/cat)}$ is the current density at each measured point of the map (considering only the positive ones, $j_{n(an)}$, for $j_{an}^{map \ average}$ and the negative ones, $j_{n(cat)}$, for $j_{cat}^{map \ average}$), and N is

the total number of points on the map. Furthermore, the noise level of machine should be considered. By measuring and analyzing the current map of a Petri dish in 3.5% NaCl solution using the same testing parameters of the maps in this work, a threshold value of 10 nA cm^{-2} was selected. Thus, only points with $|j| > 10 \text{ nA cm}^{-2}$ were calculated in Eq. (8).

Fig. 14 plots the evolution of $j_{an}^{map \ average}$ and $j_{cat}^{map \ average}$ of the SVET maps for the three coatings during the first 24 h of immersion. The CP Al coating showed relatively low and stable values as expected while the other two coatings showed much higher values. The anodic current density values of Al 2024 coating were lower than the cathodic ones during the first hour and 6 h later, the trend reversed. Meanwhile, though fluctuations were observed, the average anodic and cathodic current densities of Al 2024 coating showed an overall rising trend, which indicated the degradation of corrosion resistance in 3.5% NaCl solution. The large deviation between the average anodic and cathodic current densities could be observed for Al 5083 coating at the beginning

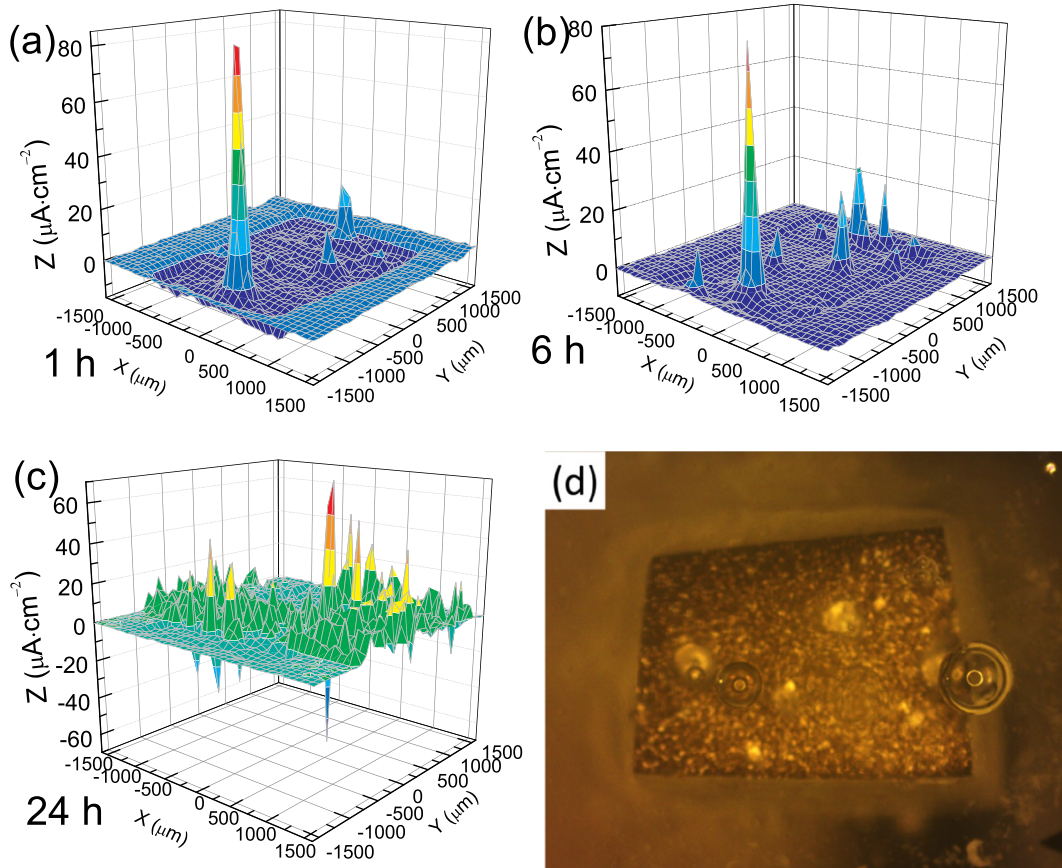


Fig. 12. SVET maps of Al 2024 coating by the beginning of exposure and after 24 h in 3.5% NaCl solution, as well as the optical image of the test surface.

of immersion. However, after 1 h of immersion, the anodic and cathodic current densities showed close values due to the decrease of the anodic current density and the increase of cathodic current density. During the subsequent immersion process, both the average anodic and cathodic current densities showed small fluctuations around $2.5 \mu\text{A}\cdot\text{cm}^{-2}$ suggesting the stable corrosion resistance of Al 5083 coating.

From the above results, the differences between the three coatings observed by SVET are obvious. CP Al coating showed the fewest pits, Al 2024 coating showed the largest pit area and the highest anodic current density while Al 5083 coating exhibited the largest number of pits. The differences between the coatings in electrochemical activity are closely associated with their alloying elements. CP Al coating showed the highest purity and nearly no precipitates were detected inside the coating. Thus, the formation of pits is difficult and the number of pit is limited. For Al 2024 coating, the galvanic cells between the Cu-rich precipitates and the α -Al matrix can accelerate the formation of pits [65], as shown in Fig. 10. Therefore, pits are easier to occur and grow. The Al 5083 particles contain dispersed Mg-rich precipitates (typically contain Mg_2Si or Al_3Mg_2) which are anodic to the Al matrix around pH 7. Thus, the number of pits in the coating is the largest. Besides the relatively low current density can be attributed to the selective leaching of Mg which produces hydroxides deposits and enrichment of the intermetallics with silicon [64], as shown in Fig. 10, thus preventing the formation of deep pits.

In conclusion, as indicated by the SVET current maps, the anodic and cathodic current density peaks of the CP Al coating decreased with increased immersion time, which meant the decrease of the pitting activity. After 24 h of immersion, numerous anodic and cathodic peaks with low current density appeared for the Al 2024 and Al 5083 coatings, which might be attributed to the micro local cell formed between the precipitates and the adjacent α -Al. Herein, an increase in the

average current density was observed for the coatings, respectively. Besides, with the expansion of the micro local cells, the pits will be interconnected and uniform corrosion on the surface may be expected.

However, some drawbacks may be encountered when using SVET on some certain conditions, since the ionic currents detected are only those that reach the probe, which is vibrating 100 μm above the surface. If the corrosion activity is weak, the ionic fluxes may not be strong enough to reach that distance or may not be distinguished from the background noise. Moreover, the probe is 50 μm in diameter, which is much larger than the precipitates inside the Al-based alloy particles, as indicated in Fig. 2. Thus, the local cathodic and anodic sites smaller than the tip diameter of the vibrating probe cannot be separated, as reported by Li et al. [66]. Also, the average anodic should be equal to the cathodic current density and hence the average current density should be zero. But deviations between them are usually observed as in this work or [67,68]. The deviations may be ascribed to the fact that the current density on an SVET map was not measured simultaneously (one scan takes ~ 10 min). In general, the values obtained by SVET will be an underestimation and it can be used as a semi-quantitative measurement to evaluate the corrosion mechanism of the cold sprayed coatings.

3.3.3. EIS spectrum and analysis

To further understand the corrosion resistance of the coatings, the electrochemical impedance spectroscopy (EIS) was measured at their OCP and the results are fitted with the corresponding equivalent electrical circuits (EEC). For comparison, the AA 2024-T3 substrate was also measured for 240 h. Fig. 14 shows the Nyquist and Bode plots evolution of the cold sprayed coatings in 3.5% NaCl solution at 0.5 h, 24 h, 480 h, 720 h, respectively. EIS measurements at other times were depicted in Fig. S5 (Supplementary material). The solid fitting lines are plotted according to the equivalent circuit shown in Fig. 16. The

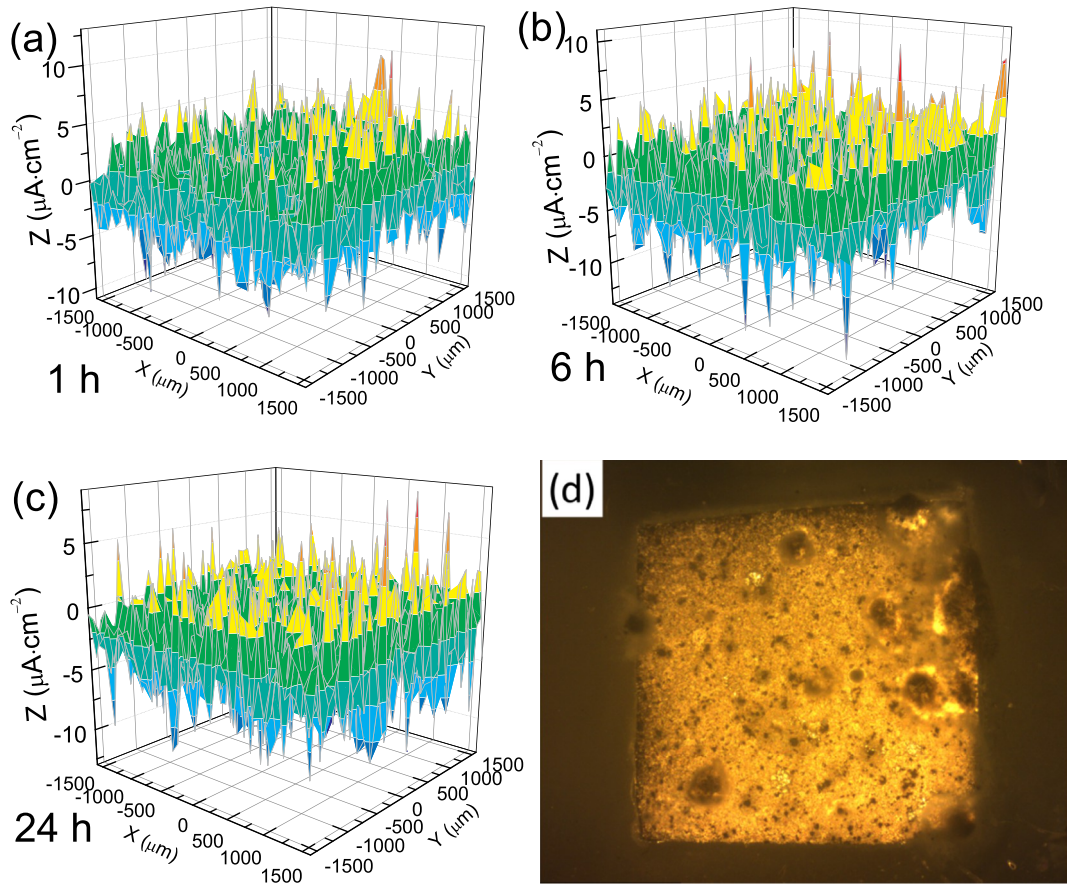


Fig. 13. SVET maps of Al 5083 coating by the beginning of exposure and after 24 h in 3.5% NaCl solution, as well as the optical image of the test surface.

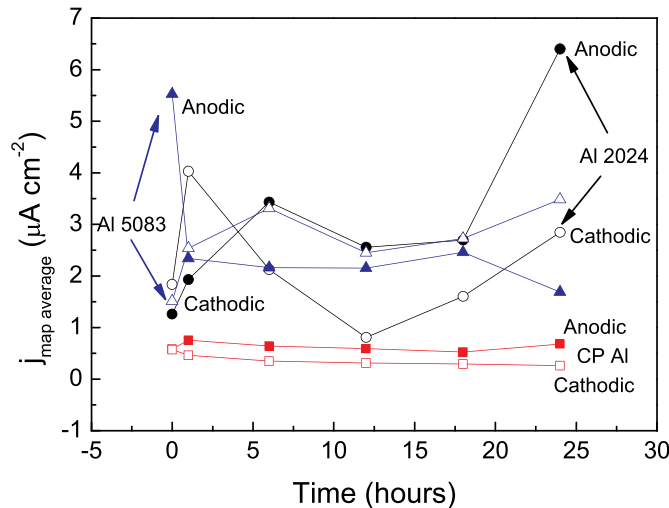


Fig. 14. Plots of the average current density in the map for CP Al, Al 2024 and Al 5083 coatings.

electrochemical corrosion processes of the sample with immersion time are defined based on the variation of the shapes of the impedance diagrams. The impedance data were fitted with appropriate equivalent circuit models to explain the different electrochemical processes occurring at the electrode-electrolyte interface.

Fig. 15(a) shows the Nyquist diagrams of the four samples after they had been immersed in 3.5% NaCl electrolyte for 0.5 h. The Nyquist plots are characterized by three time constants, a small capacitive arc at high frequencies, a depressed capacitive arc at medium frequencies,

and an inductive loop at low-frequency range. As reported by Tian et al. and Moreto et al., the one at the higher frequency refers to the original passive film on coating surface [69–72]. On the other hand, the large arc in the low-frequency range followed by an inductive loop corresponds to relaxation process due to the adsorbed species as Cl^- at active sites of the coating, resulting in the nucleation of corrosion pits [73]. The diameter of the capacitive arc is positively related to the corrosion resistance, that is, a larger diameter of the arc indicates higher electrochemical reaction resistance. At this period, Al and the Al 5083 coating exhibit similar semicircle diameter ($\sim 7 \text{ k}\Omega$) and are much larger than that of Al 2024 coating and AA 2024-T3 ($\sim 2 \text{ k}\Omega$). Moreover, the phase diagrams in Fig. 15(b) reveal that all the wave peaks are located around 20 Hz and the peak widths are similar.

After an immersion time of 24 h, as shown in Fig. 15(c), the inductive loop disappeared and the Nyquist plots consisted of a depressed capacitive arc in the medium frequency range and a nearly straight line in the low frequency. The presence of a depressed arc suggested a non-ideal behavior of the capacitor which was correlated with the passive film on coating surface, and the line in the low-frequency region was attributed to the diffusion process. Compared with 0.5 h, the diameters of all the capacitive arcs decreased obviously. Meanwhile, the maximum phase angles of the Al alloy samples in Fig. 15(d) obeyed following order: AA 2024-T3 < Al 2024 < Al 5083 < CP Al. The decrease of peak heights of the Al alloy samples compared with 0.5 h indicated that the response coating surface became less capacitive which was attributed to the chloride-induced depassivation of the passive film [14,74]. The different degradation behaviors of the passive films between the Al alloys and CP Al can be explained as follows: a) Al alloys which contain more inclusions and second phase particles, b) adsorption of Cl^- in passive film prefers at or around inclusions and second phase particles due to weaker oxide film on these sites. For

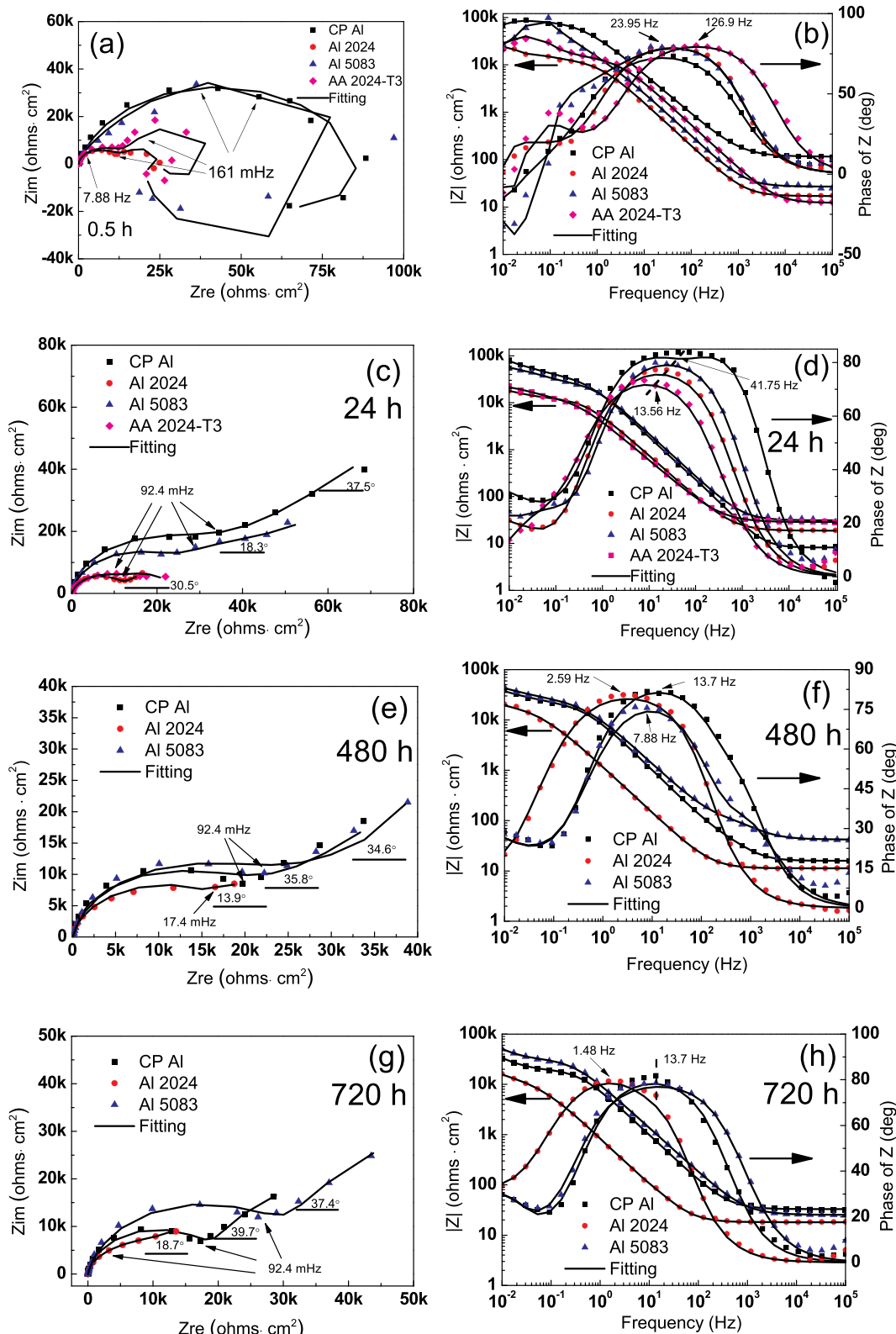


Fig. 15. The Nyquist and Bode plots evolution of the cold sprayed coatings versus time in 3.5 wt% NaCl solution at 25 °C. (a), (c), (e) and (g) is the Nyquist plots for 0.5 h, 24 h, 480 h, and 720 h, respectively, and (b), (d), (f) and (h) are the corresponding Bode plots.

24 ≤ t ≤ 240 h, the measured Nyquist plots of AA 2024-T3 showed a similar characterization (Figs. 15(a), (c), 5S): a relatively stable capacitive arc in the high-medium frequency range followed by an incomplete arc in the low frequency.

Fig. 15(e–f) shows the EIS graphics obtained at 480 h. All the EIS

Nyquist plots exhibited similar characterizations with 24 h. However, it can be seen that the straight line of Al 2024 coating was much shorter than that of 24 h. Also, the diameter of the medium-frequency capacitive arc of Al 5083 was slightly larger than that of CP Al, indicating higher corrosion resistance for Al 5083 coating. The Bode plots

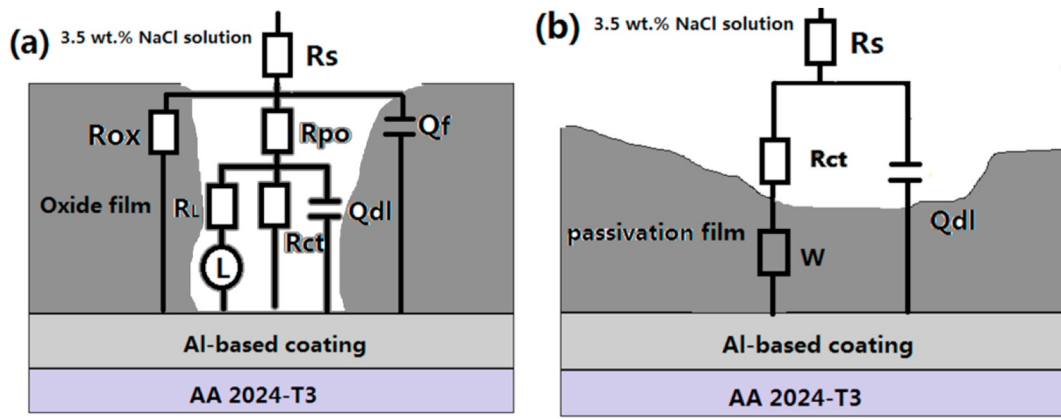


Fig. 16. Electrical equivalent circuits used to fit the EIS data. (a) for the initial stage and (b) for the stable stage (> 24 h).

Fig. 15(f) revealed that the phase angle peak of the Al 2024 coating decreased to around 2.5 Hz while CP Al and Al 5083 decreased to 13.7 Hz, which indicated the passive film on the coating surface was further fractured and degraded.

The EIS graphics at 720 h are depicted in **Fig. 15(g-h)**. The straight line of Al 2024 coating nearly disappeared due to the further combination with the medium-frequency arc. The diameter of the medium-frequency capacitive arc of CP Al continued to decrease while that of Al 5083 got further increased. Meanwhile, the slopes of the arcs of CP Al and Al 5083 coatings in the low-frequency range further increased to 0.84 and 0.76 respectively.

3.3.4. Corrosion evolution of the cold sprayed coatings

Fig. 16(a) shows the schematic representation of the corrosion and the proposed equivalent circuit in the early stage. The elements in electrical circuit are defined as follows: R_s represents the solution resistance between the working electrode and the reference, the loop $R_{ox}-C_{ox}$, respectively the resistance and capacitance of the native oxide film, R_{ct} and C_{dl} correspond to the faraday charge transfer resistance and the capacitance of the double layer, the higher the charge transfer resistance, the lower is the corrosion rate; R_{po} is the electrolytic resistance in the defects of the passive film, the inductive element L in series to R_L refers to inductance phenomenon caused by pitting corrosion [75]. The existence of the oxide film can be proved by the high fraction of O in the concentration depth profiles in Fig. 6S, with a sputtering rate of about 0.1 nm/s, thus a thickness of 6 nm was measured for all three samples. However, because R_{ox} tends to be extremely high [72], not allowing for any conduction of electrons inside the oxide film, this circuit element is usually removed from the equivalent circuit to obtain more accurate circuit fitting results. Moreover, considering

the non-ideality of the system, the capacitor C was replaced by a constant phase element (CPE). There exist two components for CPE: CPE- Y_0 and n. Y_0 is the frequency-independent admittance with a dimension being $\Omega^{-1}\text{cm}^{-2}\text{s}^{-n}$ or $\text{S cm}^{-2}\text{s}^{-n}$; n is a dimensionless index. For a capacitance element, the derivation of n from the unit is due to the heterogeneous effect which is attributed to the high roughness or non-homogeneous current distribution on the working electrode surface and when $n = 0.5$ corresponds to a diffusion process at low frequencies or porous electrode response at high frequencies [76]; or $n = 0$, to a simple resistor [75]. Thus, an equivalent electrical circuit (EEC), $R_s(Q_f(R_{po}(Q_{dl}R_{ct}(R_LL))))$, was used for fitting the experimental data. This period is the propagation stage or nucleation of pitting corrosion [8,77].

After immersed for 24 h, the inductive loop disappeared for all the samples due to the formation of corrosion products layer [75,78]. According to the schematic representation (**Fig. 16(b)**) of the corrosion procedure, an EEC of $R_s(Q_{dl}(R_{ct}W))$ was proposed for the samples, where W was the Warburg diffusive impedance. As indicated in **Fig. 15(c), (e), (g)**, the phase angles of the lines were lower than that of the typical Warburg impedance of 45° and the deviation might be attributed to the not quiescent condition of the surface or the pores on the coating surface [79]. As indicated in **Figs. 10 and 18-19**, the corrosion products layer of the Al-based coatings showed a dense microstructure and was almost continuously deposited on the coating surface. Herein, they can effectively hinder the penetration of the corrosion medium such as O, Cl⁻, to the surfaces of Al-based coatings [40,62]. Thus, the diffusion-controlled corrosion step occurred. Besides, the relatively shorter length of the line in Al 2024 coating can be ascribed to the loose and porous structure of the corrosion products layer (**Figs. 18-19**), which could not act as a fully barrier layer to isolate the electrolyte. The

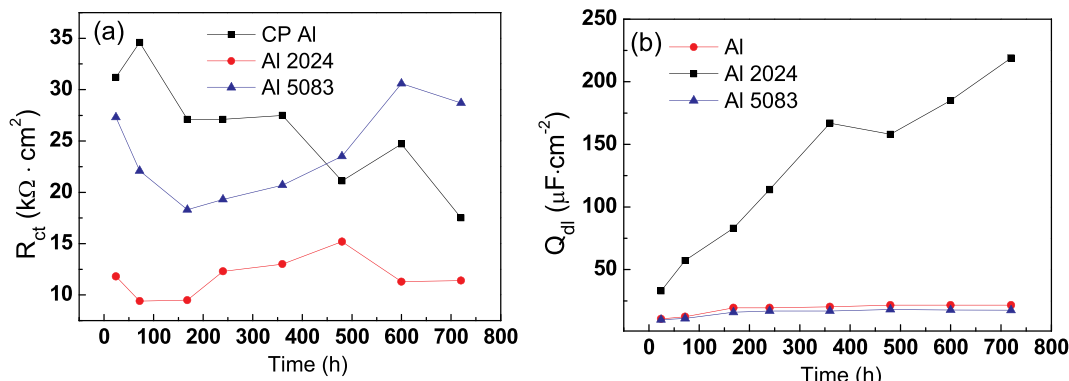


Fig. 17. Evolution of impedance fitted parameters vs. time for the cold sprayed coatings in 3.5 wt% NaCl solution. (a) the $(R_{hf} + R_{lf})$ and (b) the capacitive parameter Q_{hf} .

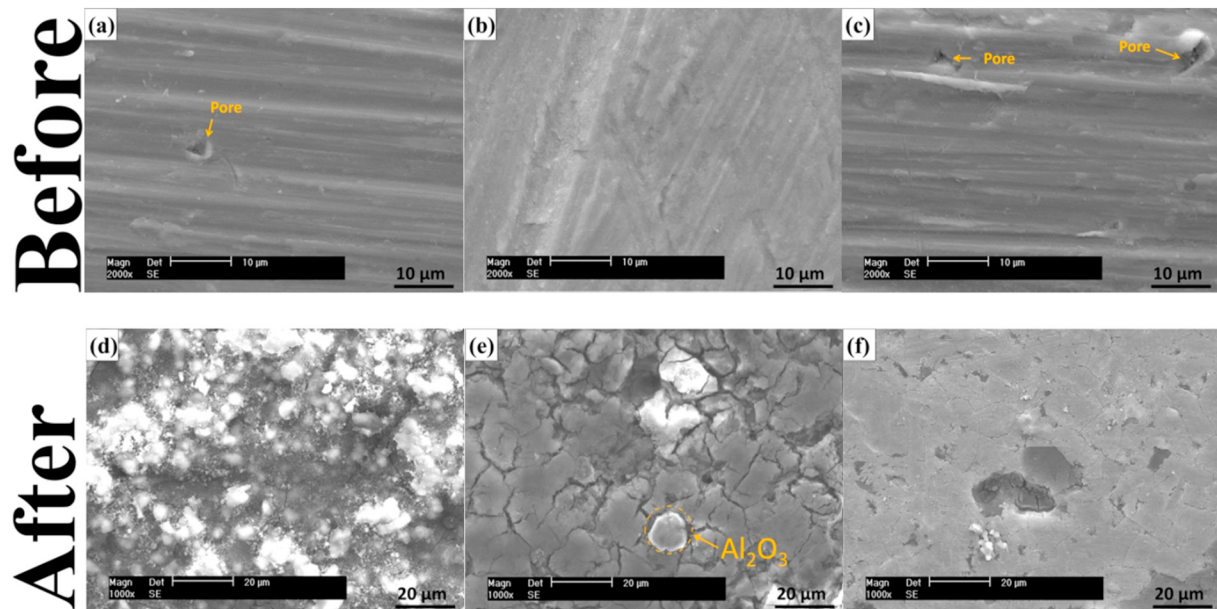


Fig. 18. The surface morphologies of the cold sprayed Al-based coatings before and after 720 h immersion: CP Al (a) (d), Al 2024 (b) (e), Al 5083 (c) (f).

fitted data with low standard error levels using the corresponding EECs are listed in Tables 1S–3S.

R_{ct} is the charge transfer resistance which is usually inversely proportional to the corrosion rate of tested samples [80,81]. The fitted values of R_{ct} in EEC versus immersion time are presented in Fig. 17(a). For CP Al coating R_{ct} resistance has slightly increased from 31.2 to 34.6 k Ω cm² up to 72 h of immersion, has stabilized at around 27.1 k Ω cm² until 360 h, and has decreased to 17 k Ω cm² till the end of the test. The slight increase of R_{ct} resistance at short immersion times could be related to the oxide formation produced by the reaction of water with aluminum, as shown in Eqs. (1), (2) and (5). As a result, the area covered by aluminum oxide increased. The following decreasing period was attributed to the attacking of Cl⁻ on the defected oxide layer (due to the impurities) which turned atom Al into Al³⁺ (see Eqs. (3) and (4)) caused the degradation of the oxide layer. The plateau meant a dynamic balance between the repassivation and de-repassivation was achieved. After 360 h, the balance was disturbed which might be attributed to the further reaction of Cl⁻ with Al³⁺, forming an oxychloride compound (see Eq. (7)) and thus increased the anodic dissolution [56,57].

The R_{ct} resistance of Al 2024 coating firstly was around 12.5 k Ω cm² after 24 h of immersion, decreased and stabilized at ~9.5 k Ω cm² up to 168 h, and increased up to ~15 k Ω cm² at 480 h, and then decreased and stabilized around ~11.3 k Ω cm² until the end of the experiment (Fig. 17(a) and Table 2S). The slight decrease of R_{ct} resistance after 24 h was mainly due to the local cells between the Cu-rich precipitations and the α -Al (see Fig. 10(b)), accelerating the fracture of the oxide layer and the dissolution of aluminum. After 168 h the R_{ct} resistance showed an increasing trend which might be due to the gradual accumulation of the corrosion products of the hydrolysis of aluminum ions covering the active areas and increasing the resistance. After 480 h, more non-disolved, cathodic Cu-rich precipitates were trapped inside the corrosion products layer (see Fig. 19(e)), possibly leading to the fracture of the brittle layer. Herein, the resistance was slightly decreased due to the penetration of electrolyte. Furthermore, the relatively low values of R_{ct} of Al 2024 coating compared with the other coatings can be attributed to the local cells between the cathodic Cu-rich precipitates and the anodic α -Al, which accelerated the dissolution of Al, as indicated in Figs. 2 and 3.

For Al 5083 coating R_{ct} resistance decreased from 27 to 18 k Ω cm² up to 168 h of immersion, then increased and stabilized at 30 k Ω cm² until 720 h. Similar to Al 2024 coating, the early decrease of resistance

may be ascribed to the local cells between the Mg-rich precipitates and the α -Al (see Fig. 10(c)). The following increase of the resistance can be associated with the accumulation of the dense corrosion products film (Fig. 19(f)).

It is widely accepted that the corrosion behavior for pure Al and its alloys is mainly determined by the second phase or precipitates, which will cause the preferential dissolution of the adjacent α -Al, thus lead to localized corrosion (pitting corrosion) [69,82–84]. Wei et al. [40] compared the corrosion rate of pure Al, AA 2219 and AA 6061 and found that pure Al showed the best corrosion resistance followed by AA 6061 coating and AA 2219. The authors attributed the difference in corrosion resistance to the different contents of second phases and impurity elements [40]. As for Al 5083, higher corrosion rate than CP Al was observed when $t < 480$ h, which was attributed to the preferential dissolution of Mg-rich precipitate as we have discussed in Section 3.3.1. After 480 h, the lower corrosion rate of Al 5083 can be ascribed to the accumulation of a dense passivation film on the coating surface (Fig. 19(f)). Ezuber et al. studied the corrosion rate of bulk AA 1100 and AA 5083 in seawater at 23 °C and found a similar trend: during the early stage, AA 5083 exhibited higher corrosion rate than AA 1100 but after 28 days, AA 1100 showed higher corrosion rate [23].

Fig. 17(b) depicts the evolution of C_{dl} with immersion time for the coatings. According to [85]:

$$C = \epsilon \epsilon_0 \cdot A \cdot d^{-1} \quad (11)$$

where C is capacitance; ϵ is dielectric permeability of the oxide layer; ϵ_0 is dielectric permeability in vacuum; A is surface area and d is layer thickness. Assuming that the surface area of the oxide does not change significantly upon immersion, the increase of capacitance may be attributed to the attack to oxide layer, making d smaller, or according to Ferreira et al. [86], the hydration of oxide layer ($Al_2O_3 \cdot xH_2O$) upon immersion, which increases the ϵ value. Since the occurrence of oxygen reduction reaction inside or around the corrosion sites, the hydroxyl ion was produced and subsequently united with Al_2O_3 and formed the hydration of oxide layer ($Al_2O_3 \cdot xH_2O$). In fact, ϵ is known to range from 9, in the case of a dry oxide, to 40, for a partially hydrated layer [85]. In Fig. 17(b), the C_{dl} values of Al 2024 coating showed an increasing trend throughout the test period, which might be attributed to the breakdown of the oxide layer, leading to the decrease of d. Meanwhile, the reactions of Al with water may increase the content of hydration which resulted in the increase of ϵ . Besides, the result also proved that the

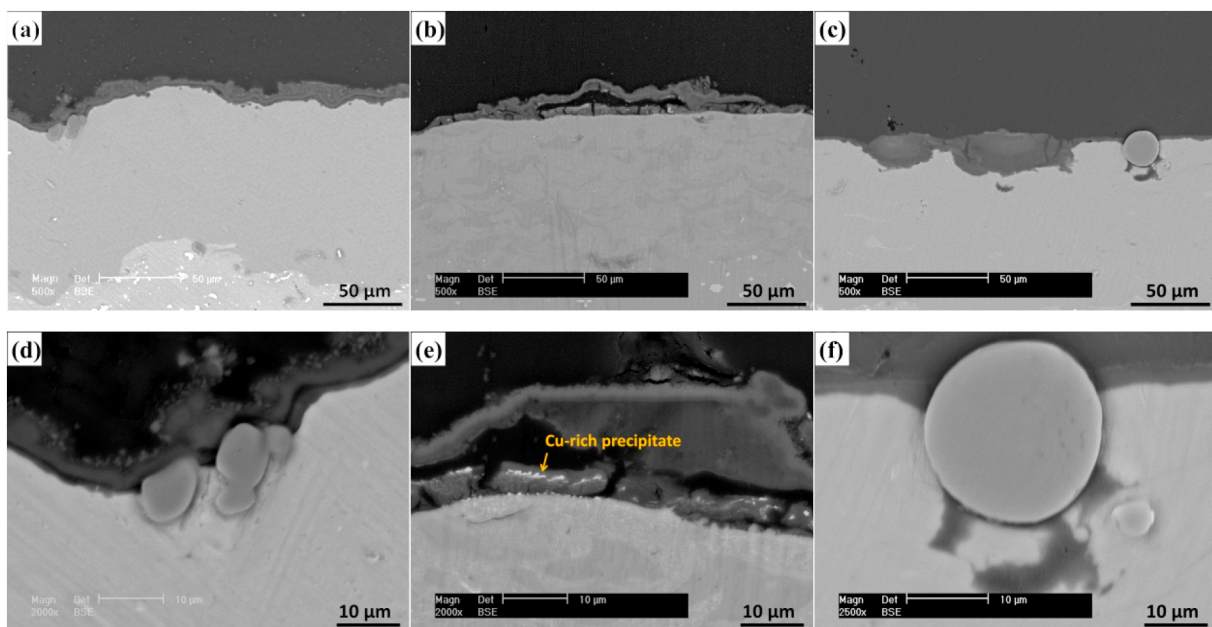


Fig. 19. Cross-sectional morphology of the coatings after immersed in 3.5% NaCl solution for 720 h, (a) for CP Al coating, (b) for Al 2024 coating and (c) for Al 5083 coating. (d), (e) and (f) are higher magnification images near the surface corresponding to (a), (b), and (c), respectively.

loose corrosion products layer on the coating surface didn't contribute to the increase of capacity and thus could provide a limited barrier effect for the coating. As for Al and Al 5083 coatings, the values of C_{dl} are much lower than Al 2024 and remained stable during the immersion test, indicating the existence of a dense and stable passive layer.

Fig. 18 shows the surface morphology of the coatings before and after the EIS test. It can be observed that there were some noticeable traces of mechanical polishing and defects in different shapes on the ground coating sheets before the test (Fig. 18(a)–(c)). After immersed for 720 h, the traces disappeared and a corrosion product layer has been deposited on the surface for each coating. In the case of CP Al coating, some loose corrosion products are dispersed on the top layer while a dense layer has been deposited underneath them (see Fig. 18(d)). Fig. 18(e) reveals that the product layer of Al 2024 coating is much looser than that of CP Al with obvious larger cracks inside it. As shown in Fig. 18(f), a dense layer with few cracks can be observed on the Al 5083 coating, which may effectively hinder the penetration of electrolyte as we have analyzed above.

Moreover, the cross-sectional morphology of the coatings after immersed in 3.5% NaCl solution for 720 h are depicted in Fig. 19. The most seriously corroded areas are selected for the observation. The images reveal that due to the dense microstructure of the coatings, the corrosion of the coatings occurred on the coating surface and the electrolyte was not able to penetrate inside the coating. No cracks or pores exist along the coating–substrate interface, indicating that the corrosion process does not affect the adhesive strength between the coating and the substrate. Besides, higher magnification images of the top coatings (Fig. 19(d)–(f)) show that a dense and continuous corrosion products layer can be observed on CP Al and Al 5083 coatings while a loose and dis-continuous layer is in the case of Al 2024, which is consistent with the observations in Fig. 18.

Taking the above analysis into consideration, we divide the corrosion process of the cold sprayed coatings into two steps. The first one was the preferential occurrence of localized anodic dissolution (pitting corrosion) of the Al-based coatings or the anodic precipitates (Mg-rich) at the defects sites of the oxide film or around the local cells after the coatings were immersed in the electrolyte. Generally, with the extension of time, the pitting corrosion can gradually spread throughout the entire surface and the corrosion type will change from pitting to

uniform corrosion in neutral environments as observed in Fig. 19. Similar changes were also observed in [40,82]. In the second step, corrosion along the coating thickness direction continuously developed leading to the accumulation of corrosion products (Fig. 19).

4. Conclusion

In this paper, dense Al-based coatings were successfully deposited using low-pressure cold spray technique for defects repair and corrosion protection of AA2024-T3. Spherical Al_2O_3 particles were blended into the feedstock powers to produce enhanced shot peening effects. The mechanical and corrosion properties of the resultant composite coatings were examined.

All the coatings exhibit dense microstructure with low porosity, very few trapped Al_2O_3 particles. Meanwhile, the Al 5083 coating possessed the best overall mechanical properties such as the highest microhardness, cohesive strength, and residual compressive stress while the CP Al coating showed the poorest.

The E_{OCP} observation results reveal that all the coatings exhibit lower E_{OCP} values than the AA2024-T3 substrate. The cyclic polarization measurements show that pitting is the major corrosion form for the tested coatings. The CP Al coating exhibited the highest pitting resistance and repassivation ability among the three coatings while Al 2024 coating showed the poorest.

SVET results reveal that the CP Al coating showed the lowest pitting activity while Al 2024 coating showed the highest during the 24 h immersion in 3.5% NaCl aqueous solution. For the EIS tests in 3.5% NaCl aqueous solution, Al 2024 coating showed the highest corrosion rate throughout the testing time. CP Al coating showed the lowest corrosion rate at $t < 480$ h, however, after that Al 5083 coating showed the lowest corrosion rate until the end of the test.

According to the results of the present work, the Al 5083 coating exhibits an excellent combination of mechanical and anti-corrosion properties and maybe a better choice for the components repair and protection. Furthermore, spherical Al_2O_3 powder should be taken into consideration as a reinforcement phase in cold sprayed metal matrix composite coatings.

CRediT authorship contribution statement

Zhichao Zhang:Conceptualization, Methodology, Software, Investigation, Writing - original draft.**Fuchun Liu:**Supervision, Resources, Writing - review & editing.**En-Hou Han:**Resources.**Long Xu:**Formal analysis.

Declaration of competing interest

We declare that we have no financial and personal relationships with other people or organizations that can inappropriately influence our work. There is no professional or other personal interest of any nature or kind in any product, service and/or company that could be construed as influencing the position presented in, or the review of, the manuscript entitled.

Acknowledgments

The authors would like to acknowledge the Special Scientific Research on Civil Aircraft (MJ-2016-F-07).

Appendix A. Supplementary data

Supplementary data to this article can be found online at <https://doi.org/10.1016/j.surfcoat.2020.125372>.

References

- [1] S. Dymek, M. Dollar, TEM investigation of age-hardenable Al 2519 alloy subjected to stress corrosion cracking tests, Mater. Chem. Phys. 81 (2) (2003) 286–288, [https://doi.org/10.1016/S0254-0584\(02\)00603-X](https://doi.org/10.1016/S0254-0584(02)00603-X).
- [2] K.H. Na, S.I. Pyun, Comparison of susceptibility to pitting corrosion of AA2024-T4, AA7075-T651 and AA7475-T761 aluminum alloys in neutral chloride solutions using electrochemical noise analysis, Corros. Sci. 50 (1) (2008) 248–258, <https://doi.org/10.1016/j.corsci.2007.05.028>.
- [3] M.R. Rokni, et al., An investigation into the hot deformation characteristics of 7075 aluminum alloy, Mater. Des. 32 (4) (2011) 2339–2344, <https://doi.org/10.1016/j.matdes.2010.12.047>.
- [4] S. Liu, et al., Enhanced corrosion resistance of 5083 aluminum alloy by refining with nano-CeB6/Al inoculant, Appl. Surf. Sci. 484 (2019) 403–408, <https://doi.org/10.1016/j.apsusc.2019.03.283>.
- [5] Z. Nacer, et al., Pretreatment effects on the electrochemical responses for aluminum-magnesium alloy AA5083 corrosion behaviour, J. SOLID STATE ELECTR 14 (9) (2010) 1705–1711, <https://doi.org/10.1007/s10008-010-1021-0>.
- [6] K.S. Ghosh, M. Hilal, S. Bose, Corrosion behavior of 2024 Al-Cu-Mg alloy of various tempers, Trans. Nonferrous Metals Soc. China 23 (11) (2013) 3215–3227, [https://doi.org/10.1016/S1003-6326\(13\)62856-3](https://doi.org/10.1016/S1003-6326(13)62856-3).
- [7] J.F. Li, et al., Localized corrosion mechanism of 2 × × -series Al alloy containing S (Al2CuMg) and θ'(Al2Cu) precipitates in 4.0% NaCl solution at pH 6.1, Mater. Chem. Phys. 91 (2) (2005) 325–329, <https://doi.org/10.1016/j.matchemphys.2004.11.034>.
- [8] M.A. Jingling, et al., The corrosion behaviour of Al-Zn-In-Mg-Ti alloy in NaCl solution, Corros. Sci. 52 (2) (2010) 534–539, <https://doi.org/10.1016/j.corsci.2009.10.010>.
- [9] W.A. Badawy, F.M. Al-Kharafi, A.S. El-Azab, Electrochemical behaviour and corrosion inhibition of Al, Al-6061 and Al-Cu in neutral aqueous solutions, Corros. Sci. 41 (4) (1999) 709–727, [https://doi.org/10.1016/S0010-938X\(98\)00145-0](https://doi.org/10.1016/S0010-938X(98)00145-0).
- [10] C.M. Abreu, et al., Evolution of corrosion behavior for AA7075 aluminum alloy implanted with nitrogen, Nucl. Instrum. Methods Phys. Res., Sect. B 442 (2019) 1–12, <https://doi.org/10.1016/j.nimb.2019.01.013>.
- [11] H. Kreye, T. Stoltenhoff, Cold spraying-a study of process and coating characteristics, Int. J. Sci. Res. Dev. 2 (6) (2000) 614–615.
- [12] C.J. Li, et al., A theoretical model for prediction of deposition efficiency in cold spraying, Thin Solid Films 489 (1) (2005) 79–85, <https://doi.org/10.1016/j.tsf.2005.05.002>.
- [13] T.H. Van Steenkiste, Kinetic spray: a new coating process, Key Eng. Mater. 197 (1975) (2001) 59–86, <https://doi.org/10.4028/www.scientific.net/KEM.197.59>.
- [14] F.S.D. Silva, et al., Corrosion characteristics of cold gas spray coatings of reinforced aluminum deposited onto carbon steel, Corros. Sci. 114 (2017) 57–71, <https://doi.org/10.1016/j.corsci.2016.10.019>.
- [15] T. Novoselova, et al., Experimental study of titanium/aluminium deposits produced by cold gas dynamic spray, Surf. Coat. Technol. 200 (8) (2006) 2775–2783, <https://doi.org/10.1016/j.surfcoat.2004.10.133>.
- [16] P. Cavaliere, A. Silvello, Processing parameters affecting cold spray coatings performances, Int. J. Adv. Manuf. Technol. 71 (1–4) (2014) 263–277, <https://doi.org/10.1007/s00170-013-5465-0>.
- [17] P. Cavaliere, A. Silvello, Crack repair in aerospace aluminum alloy panels by cold spray, J. Therm. Spray Technol. 26 (4) (2017) 661–670, <https://doi.org/10.1007/s11666-017-0534-9>.
- [18] M.R. Rokni, et al., Review of relationship between particle deformation, coating microstructure, and properties in high-pressure cold spray, J. Therm. Spray Technol. 26 (6) (2017) 1308–1355, <https://doi.org/10.1007/s11666-017-0575-0>.
- [19] M.F. Smith, 3 - comparing cold spray with thermal spray coating technologies, in: V.K. Champagne (Ed.), *The Cold Spray Materials Deposition Process*, Woodhead Publishing, 2007, pp. 43–61.
- [20] J. Karthikeyan, 4 – the advantages and disadvantages of the cold spray coating process, *Cold Spray Materials Deposition Process*, 2007, pp. 62–71.
- [21] Y. Wang, et al., Effects of ceramic particle size on microstructure and the corrosion behavior of cold sprayed SiC p/Al 5056 composite coatings, Surf. Coat. Technol. 315 (2017) 314–325, <https://doi.org/10.1016/j.surfcoat.2017.02.047>.
- [22] E.J.T. Pialago, O.K. Kwon, C.W. Park, Cold spray deposition of mechanically alloyed ternary Cu-CNT-SiC composite powders, Ceram. Int. 41 (5) (2015) 6764–6775, <https://doi.org/10.1016/j.ceraint.2015.01.123>.
- [23] H. Ezuber, A. El-Houd, F. El-Shawesh, A study on the corrosion behavior of aluminum alloys in seawater, Mater. Des. 29 (4) (2008) 801–805, <https://doi.org/10.1016/j.matdes.2007.01.021>.
- [24] B. Ralph, H.C. Yuen, W.B. Lee, The processing of metal matrix composites — an overview, J. Mater. Process. Technol. 63 (1–3) (1997) 339–353, [https://doi.org/10.1016/S0924-0136\(96\)02645-3](https://doi.org/10.1016/S0924-0136(96)02645-3).
- [25] Y.-K. Wei, et al., Corrosion resistant nickel coating with strong adhesion on AZ31B magnesium alloy prepared by an in-situ shot-peening-assisted cold spray, Corros. Sci. 138 (2018) 105–115, <https://doi.org/10.1016/j.corsci.2018.04.018>.
- [26] H. Zhou, et al., Local microstructure inhomogeneity and gas temperature effect in in-situ shot-peening assisted cold-sprayed Ti-6Al-4V coating, J. Alloys Compd. 766 (2018) 694–704, <https://doi.org/10.1016/j.jallcom.2018.07.009>.
- [27] Z. Zhang, et al., Effects of Al2O3 on the microstructures and corrosion behavior of low-pressure cold gas sprayed Al 2024-Al2O3 composite coatings on AA 2024-T3 substrate, Surf. Coat. Technol. 370 (2019) 53–68, <https://doi.org/10.1016/j.surfcoat.2019.04.082>.
- [28] M. Winnicki, et al., The bond strength of Al + Al2O3 cermet coatings deposited by low-pressure cold spraying, Arch. Civil Mech. Eng. 16 (4) (2016) 743–752, <https://doi.org/10.1016/j.acme.2016.04.014>.
- [29] Y. Tao, et al., Effect of α-Al 2 O 3 on the properties of cold sprayed Al/α-Al 2 O 3 composite coatings on AZ91D magnesium alloy, Appl. Surf. Sci. 256 (1) (2009) 261–266, <https://doi.org/10.1016/j.apsusc.2009.08.012>.
- [30] J.M. Shockley, et al., The influence of Al2O3 particle morphology on the coating formation and dry sliding wear behavior of cold sprayed Al-Al2O3 composites, Surf. Coat. Technol. 270 (2015) 324–333, <https://doi.org/10.1016/j.surfcoat.2015.01.057>.
- [31] M. Yandouzi, et al., Aircraft skin restoration and evaluation, J. Therm. Spray Technol. 23 (8) (2014) 1281–1290, <https://doi.org/10.1007/s11666-014-0130-1>.
- [32] P. Sirvent, et al., Effect of higher deposition temperatures on the microstructure and mechanical properties of Al 2024 cold sprayed coatings, Surf. Coat. Technol. 337 (2018) 461–470, <https://doi.org/10.1016/j.surfcoat.2018.01.055>.
- [33] K. Yang, et al., Cold sprayed AA2024/Al 2 O 3 metal matrix composites improved by friction stir processing: microstructure characterization, mechanical performance and strengthening mechanisms, J. Alloys Compd. 736 (2018) 115–123, <https://doi.org/10.1016/j.jallcom.2017.11.132>.
- [34] Y. Wang, et al., Microstructure and corrosion behavior of cold sprayed SiCp/Al 5056 composite coatings, Surf. Coat. Technol. 251 (2014) 264–275, <https://doi.org/10.1016/j.surfcoat.2014.04.036>.
- [35] Standard Guide for Metallographic Preparation of Thermal Spray Coatings American Standard of Testing Materials, West Conshohocken, (2008).
- [36] Standard Test Method for Determining Area Percentage Porosity of Thermal Spray Coatings American Standard of Testing Materials, West Conshohocken, 2014.
- [37] R. Huang, et al., The effects of heat treatment on the mechanical properties of cold-sprayed coatings, Surf. Coat. Technol. 261 (2015) 278–288.
- [38] E. Atkins, Elements of X-ray diffraction, Phys. Today 10 (3) (1978) 572.
- [39] B. Zheng, et al., Gas atomization of amorphous aluminum: part I. Thermal behavior calculations, Metall. Mater. Trans. B 40 (5) (2009) 768–778, <https://doi.org/10.1007/s11663-009-9276-5>.
- [40] Y.-K. Wei, et al., Deposition of fully dense Al-based coatings via in-situ micro-forging assisted cold spray for excellent corrosion protection of AZ31B magnesium alloy, J. Alloys Compd. 806 (2019) 1116–1126, <https://doi.org/10.1016/j.jallcom.2019.07.279>.
- [41] S. Ngai, et al., Saltwater corrosion behavior of cold sprayed AA7075 aluminum alloy coatings, Corros. Sci. 130 (2018) 231–240, <https://doi.org/10.1016/j.corsci.2017.10.033>.
- [42] T. Liu, et al., Microstructural analysis of gas atomized Al-Cu alloy feedstock powders for cold spray deposition, Surf. Coat. Technol. 350 (2018) 621–632, <https://doi.org/10.1016/j.surfcoat.2018.07.006>.
- [43] Y.K. Wei, et al., Optimization of in-situ shot-peening-assisted cold spraying parameters for full corrosion protection of mg alloy by fully dense Al-based alloy coating, J. Therm. Spray Technol. 26 (1–2) (2017) 173–183, <https://doi.org/10.1007/s11666-016-0492-7>.
- [44] H. Getu, J.K. Spelt, M. Papini, Conditions leading to the embedding of angular and spherical particles during the solid particle erosion of polymers, Wear 292–293 (2012) 159–168, <https://doi.org/10.1016/j.wear.2012.05.017>.
- [45] X.-T. Luo, et al., Microstructure and mechanical property of Ti and Ti6Al4V prepared by an in-situ shot peening assisted cold spraying, Mater. Des. 85 (2015) 527–533, <https://doi.org/10.1016/j.matdes.2015.07.015>.
- [46] H. Koivuluoto, P. Vuoristo, Effect of powder type and composition on structure and mechanical properties of Cu + Al2O3 coatings prepared by using low-pressure cold

- spray process, *J. Therm. Spray Technol.* 19 (5) (2010) 1081–1092, <https://doi.org/10.1007/s11666-010-9491-2>.
- [47] B. Guo, et al., The correction of temperature-dependent Vickers hardness of cemented carbide base on the developed high-temperature hardness tester, *J. Mater. Process. Technol.* 255 (2018) 426–433, <https://doi.org/10.1016/j.jmatprotec.2017.12.041>.
- [48] X.-T. Luo, et al., High velocity impact induced microstructure evolution during deposition of cold spray coatings: a review, *Surf. Coat. Technol.* 254 (2014) 11–20, <https://doi.org/10.1016/j.surfcoat.2014.06.006>.
- [49] G. Shayegan, et al., Residual stress induced by cold spray coating of magnesium AZ31B extrusion, *Mater. Design* 60 (2014) 72–84, <https://doi.org/10.1016/j.matdes.2014.03.054>.
- [50] J. Zhang, D. Kong, Effect of laser remelting on microstructure and immersion corrosion of cold-sprayed aluminum coating on S355 structural steel, *Opt. Laser Technol.* 106 (2018) 348–356, <https://doi.org/10.1016/j.optlastec.2018.04.026>.
- [51] K. Spencer, et al., Residual stresses in cold spray Al coatings: the effect of alloying and of process parameters, *Surf. Coat. Technol.* 206 (19) (2012) 4249–4255, <https://doi.org/10.1016/j.surfcoat.2012.04.034>.
- [52] O.P. Oladijo, A.M. Venter, L.A. Cornish, Correlation between residual stress and abrasive wear of WC-17Co coatings, *Int. J. Refract. Met. Hard Mater.* 44 (2014) 68–76, <https://doi.org/10.1016/j.ijrmhm.2014.01.009>.
- [53] U. Trdan, J. Grum, Evaluation of corrosion resistance of AA6082-T651 aluminium alloy after laser shock peening by means of cyclic polarisation and EIS methods, *Corros. Sci.* 59 (2012) 324–333, <https://doi.org/10.1016/j.corsci.2012.03.019>.
- [54] O. Meydanoglu, B. Jodoin, E.S. Kayali, Microstructure, mechanical properties and corrosion performance of 7075 Al matrix ceramic particle reinforced composite coatings produced by the cold gas dynamic spraying process, *Surf. Coat. Technol.* 235 (2013) 108–116, <https://doi.org/10.1016/j.surfcoat.2013.07.020>.
- [55] E. McCafferty, Sequence of steps in the pitting of aluminum by chloride ions, *Corros. Sci.* 45 (7) (2003) 1421–1438, [https://doi.org/10.1016/S0010-938X\(02\)00231-7](https://doi.org/10.1016/S0010-938X(02)00231-7).
- [56] D. Wang, et al., Electrochemical and DFT studies of quinoline derivatives on corrosion inhibition of AA5052 aluminum alloy in NaCl solution, *Appl. Surf. Sci.* 357 (2015) 2176–2183, <https://doi.org/10.1016/j.apsusc.2015.09.206>.
- [57] E.M. Sherif, S.-M. Park, Effects of 1,4-naphthoquinone on aluminum corrosion in 0.50M sodium chloride solutions, *Electrochim. Acta* 51 (7) (2006) 1313–1321, <https://doi.org/10.1016/j.electacta.2005.06.018>.
- [58] Z. Szklarska-Smialowska, Pitting corrosion of aluminum, *Corros. Sci.* 41 (9) (1999) 1743–1767, [https://doi.org/10.1016/S0010-938X\(99\)00012-8](https://doi.org/10.1016/S0010-938X(99)00012-8).
- [59] J. Ma, et al., Electrochemical polarization and corrosion behavior of Al-Zn-In based alloy in acidity and alkalinity solutions, *Int. J. Hydrom. Energy* 38 (34) (2013) 14896–14902, <https://doi.org/10.1016/j.ijhydene.2013.09.046>.
- [60] M.A. Amin, A newly synthesized glycine derivative to control uniform and pitting corrosion processes of Al induced by SCN anions – chemical, electrochemical and morphological studies, *Corros. Sci.* 52 (10) (2010) 3243–3257, <https://doi.org/10.1016/j.corsci.2010.05.041>.
- [61] G.E. Kiourtsidis, S.M. Skolianos, E.G. Pavlidou, A study on pitting behaviour of AA2024/SiC p composites using the double cycle polarization technique, *Corros. Sci.* 41 (6) (1999) 1185–1203, [https://doi.org/10.1016/S0010-938X\(98\)00179-6](https://doi.org/10.1016/S0010-938X(98)00179-6).
- [62] Y. Liu, G.Z. Meng, Y.F. Cheng, Electronic structure and pitting behavior of 3003 aluminum alloy passivated under various conditions, *Electrochim. Acta* 54 (17) (2009) 4155–4163, <https://doi.org/10.1016/j.electacta.2009.02.058>.
- [63] Y. Huang, et al., Effect of homogenization on the corrosion behavior of 5083-H321 aluminum alloy, *J. Alloys Compd.* 673 (2016) 73–79, <https://doi.org/10.1016/j.jallcom.2016.02.228>.
- [64] M. Trueba, S.P. Trasatti, Study of Al alloy corrosion in neutral NaCl by the pitting scan technique, *Mater. Chem. Phys.* 121 (3) (2010) 523–533, <https://doi.org/10.1016/j.matchemphys.2010.02.022>.
- [65] G.S. Chen, M. Gao, R.P. Wei, Microconstituent-induced pitting corrosion in aluminum alloy 2024-T3, *Corrosion* 52 (1) (1996) 8–15, <https://doi.org/10.5006/1.3292099>.
- [66] Y. Li, et al., pH-dependent electrochemical behaviour of Al3Mg2 in NaCl solution, *Appl. Surf. Sci.* 467–468 (2019) 619–633, <https://doi.org/10.1016/j.apsusc.2018.10.193>.
- [67] M. Yan, et al., SVET method for characterizing anti-corrosion performance of metal-rich coatings, *Corros. Sci.* 52 (8) (2010) 2636–2642, <https://doi.org/10.1016/j.corsci.2010.04.012>.
- [68] C.F. Glover, et al., Performance of Mg-Sn surface alloys for the sacrificial cathodic protection of Mg alloy AZ31B-H24, *Corros. Sci.* 149 (2019) 195–206, <https://doi.org/10.1016/j.corsci.2019.01.015>.
- [69] J.A. Moreto, et al., SVET, SKP and EIS study of the corrosion behaviour of high strength Al and Al-Li alloys used in aircraft fabrication, *Corros. Sci.* 84 (84) (2014) 30–41, <https://doi.org/10.1016/j.corsci.2014.03.001>.
- [70] W. Tian, et al., Pitting corrosion of naturally aged AA 7075 aluminum alloys with bimodal grain size, *Corros. Sci.* 113 (2016) 1–16, <https://doi.org/10.1016/j.corsci.2016.09.013>.
- [71] J. Zhang, et al., Corrosion behaviors of Zn/Al-Mn alloy composite coatings deposited on magnesium alloy AZ31B (Mg-Al-Zn), *Electrochim. Acta* 55 (2) (2009) 560–571, <https://doi.org/10.1016/j.electacta.2009.09.026>.
- [72] J. Ryl, et al., Effect of native air-formed oxidation on the corrosion behavior of AA 7075 aluminum alloys, *Corros. Sci.* 87 (5) (2014) 150–155, <https://doi.org/10.1016/j.corsci.2014.06.022>.
- [73] J. He, J. Wen, X. Li, Effects of precipitates on the electrochemical performance of Al sacrificial anode, *Corros. Sci.* 53 (5) (2011) 1948–1953, <https://doi.org/10.1016/j.corsci.2011.02.016>.
- [74] C.Q. Ye, et al., EIS analysis on chloride-induced corrosion behavior of reinforcement steel in simulated carbonated concrete pore solutions, *J. Electroanal. Chem.* 688 (4) (2013) 275–281, <https://doi.org/10.1016/j.jelechem.2012.09.012>.
- [75] Q. Jiang, et al., Corrosion behavior of arc sprayed Al-Zn-Si-RE coatings on mild steel in 3.5wt% NaCl solution, *Electrochim. Acta* 115 (2014) 644–656, <https://doi.org/10.1016/j.electacta.2013.09.156>.
- [76] M.E.O.B. Tribollet, *Electrochemical Impedance Spectroscopy*, 2nd edition, (2017).
- [77] C. Cao, H. Lin, Effect of Cl⁻ ion on the impedance of passive-film-covered electrodes, *J. Chin. Soc. Corr. Protect.* 9 (4) (1989) 261–270.
- [78] X. Yunchang, et al., Corrosion resistance and cytocompatibility of biodegradable surgical magnesium alloy coated with hydrogenated amorphous silicon, *J. Biomed. Mater. Res. A* 89A (3) (2010) 717–726, <https://doi.org/10.1002/jbm.a.32006>.
- [79] D.D. Macdonald, Reflections on the history of electrochemical impedance spectroscopy, *Electrochim. Acta* 51 (8) (2006) 1376–1388, <https://doi.org/10.1016/j.electacta.2005.02.107>.
- [80] M. Frederico, et al., Silica nanocontainers for active corrosion protection, *Nanoscale* 4 (4) (2012) 1287–1298, <https://doi.org/10.1039/C2nr11536k>.
- [81] M. Mahdavian, M.M. Attar, Another approach in analysis of paint coatings with EIS measurement: phase angle at high frequencies, *Corros. Sci.* 48 (12) (2006) 4152–4157, <https://doi.org/10.1016/j.corsci.2006.03.012>.
- [82] M. Cao, et al., Electrochemical corrosion behavior of 2A02 Al alloy under an accelerated simulation marine atmospheric environment, *J. Mater. Sci. Technol.* 35 (4) (2019) 651–659, <https://doi.org/10.1016/j.jmst.2018.09.060>.
- [83] J. Liu, et al., Effect of surface abrasion on pitting corrosion of Al-Li alloy, *Corros. Sci.* 138 (2018) 75–84, <https://doi.org/10.1016/j.corsci.2018.04.010>.
- [84] J. Kang, et al., In-situ investigation on the pitting corrosion behavior of friction stir welded joint of AA2024-T3 aluminium alloy, *Corros. Sci.* 52 (2) (2010) 620–626, <https://doi.org/10.1016/j.corsci.2009.10.027>.
- [85] F.J. Martin, et al., Impedance studies of the passive film on aluminium, *Corros. Sci.* 47 (12) (2005) 3187–3201, <https://doi.org/10.1016/j.corsci.2005.05.058>.
- [86] S.C. Ferreira, et al., Corrosion behaviour of Al/Al₃Ti and Al/Al₃Zr functionally graded materials produced by centrifugal solid-particle method: influence of the intermetallics volume fraction, *Corros. Sci.* 53 (6) (2011) 2058–2065, <https://doi.org/10.1016/j.corsci.2011.02.010>.